

Mesoscale Modeling of Nonlinear Elasticity and Fracture in Ceramic Polycrystals Under Dynamic Shear and Compression

by J. D. Clayton, R. H. Kraft, and R. B. Leavy

ARL-RP-386

August 2012

A reprint from the International Journal of Solids and Structures, Vol. 49, pp. 2686–2702, 2012.

NOTICES

Disclaimers

The findings in this report are not to be construed as an official Department of the Army position unless so designated by other authorized documents.

Citation of manufacturer's or trade names does not constitute an official endorsement or approval of the use thereof.

Destroy this report when it is no longer needed. Do not return it to the originator.

Army Research Laboratory

Aberdeen Proving Ground, MD 21005-5069

ARL-RP-386**August 2012**

Mesoscale Modeling of Nonlinear Elasticity and Fracture in Ceramic Polycrystals Under Dynamic Shear and Compression

J. D. Clayton, R. H. Kraft, and R. B. Leavy
Weapons and Materials Research Directorate, ARL

A reprint from the *International Journal of Solids and Structures*, Vol. 49, pp. 2686–2702, 2012.

REPORT DOCUMENTATION PAGE				Form Approved OMB No. 0704-0188	
Public reporting burden for this collection of information is estimated to average 1 hour per response, including the time for reviewing instructions, searching existing data sources, gathering and maintaining the data needed, and completing and reviewing the collection information. Send comments regarding this burden estimate or any other aspect of this collection of information, including suggestions for reducing the burden, to Department of Defense, Washington Headquarters Services, Directorate for Information Operations and Reports (0704-0188), 1215 Jefferson Davis Highway, Suite 1204, Arlington, VA 22202-4302. Respondents should be aware that notwithstanding any other provision of law, no person shall be subject to any penalty for failing to comply with a collection of information if it does not display a currently valid OMB control number. PLEASE DO NOT RETURN YOUR FORM TO THE ABOVE ADDRESS.					
1. REPORT DATE (DD-MM-YYYY) August 2012		2. REPORT TYPE Reprint		3. DATES COVERED (From - To) January 2011–March 2012	
4. TITLE AND SUBTITLE Mesoscale Modeling of Nonlinear Elasticity and Fracture in Ceramic Polycrystals Under Dynamic Shear and Compression				5a. CONTRACT NUMBER	
				5b. GRANT NUMBER	
				5c. PROGRAM ELEMENT NUMBER	
6. AUTHOR(S) J. D. Clayton, R. H. Kraft, and R. B. Leavy				5d. PROJECT NUMBER AH80	
				5e. TASK NUMBER	
				5f. WORK UNIT NUMBER	
7. PERFORMING ORGANIZATION NAME(S) AND ADDRESS(ES) U.S. Army Research Laboratory ATTN: RDRL-WMP-B Aberdeen Proving Ground, MD 21005-5069				8. PERFORMING ORGANIZATION REPORT NUMBER ARL-RP-386	
9. SPONSORING/MONITORING AGENCY NAME(S) AND ADDRESS(ES)				10. SPONSOR/MONITOR'S ACRONYM(S)	
				11. SPONSOR/MONITOR'S REPORT NUMBER(S)	
12. DISTRIBUTION/AVAILABILITY STATEMENT					
13. SUPPLEMENTARY NOTES A reprint from the <i>International Journal of Solids and Structures</i> , Vol. 49, pp. 2686–2702, 2012.					
14. ABSTRACT Dynamic deformation and failure mechanisms in polycrystalline ceramics are investigated through constitutive modeling and numerical simulation. Two ceramics are studied: silicon carbide (SiC, hexagonal crystal structure) and aluminum oxynitride (AlON, cubic crystal structure). Three dimensional finite element simulations incorporate nonlinear anisotropic elasticity for behavior of single crystals within polycrystalline aggregates, cohesive zone models for intergranular fracture, and contact interactions among fractured interfaces. Boundary conditions considered include uniaxial strain compression, uniaxial stress compression, and shear with varying confinement, all at high loading rates. Results for both materials demonstrate shear-induced dilatation and increasing shear strength with increasing confining pressure. Failure statistics for unconfined loading exhibit a smaller Weibull modulus (corresponding to greater scatter in peak failure strength) in AlON than in SiC, likely a result of lower prescribed cohesive fracture strength and greater elastic anisotropy in the former. In both materials, the predicted Weibull modulus tends to decrease with an increasing number of grains contained in the simulated microstructure.					
15. SUBJECT TERMS elasticity, fracture, finite elements, ceramics, polycrystals, SiC, AlON					
16. SECURITY CLASSIFICATION OF:			17. LIMITATION OF ABSTRACT UU	18. NUMBER OF PAGES 24	19a. NAME OF RESPONSIBLE PERSON J. D. Clayton
a. REPORT Unclassified	b. ABSTRACT Unclassified	c. THIS PAGE Unclassified			19b. TELEPHONE NUMBER (Include area code) 410-278-6146



Mesoscale modeling of nonlinear elasticity and fracture in ceramic polycrystals under dynamic shear and compression

J.D. Clayton ^{*}, R.H. Kraft, R.B. Leavy

RDRL-WMP-B, US Army Research Laboratory, Aberdeen Proving Ground, MD 21005-5066, USA

ARTICLE INFO

Article history:

Received 6 May 2011

Received in revised form 1 March 2012

Available online 9 June 2012

Keywords:

Elasticity

Fracture

Finite elements

Ceramics

Polycrystals

ABSTRACT

Dynamic deformation and failure mechanisms in polycrystalline ceramics are investigated through constitutive modeling and numerical simulation. Two ceramics are studied: silicon carbide (SiC, hexagonal crystal structure) and aluminum oxynitride (AlON, cubic crystal structure). Three dimensional finite element simulations incorporate nonlinear anisotropic elasticity for behavior of single crystals within polycrystalline aggregates, cohesive zone models for intergranular fracture, and contact interactions among fractured interfaces. Boundary conditions considered include uniaxial strain compression, uniaxial stress compression, and shear with varying confinement, all at high loading rates. Results for both materials demonstrate shear-induced dilatation and increasing shear strength with increasing confining pressure. Failure statistics for unconfined loading exhibit a smaller Weibull modulus (corresponding to greater scatter in peak failure strength) in AlON than in SiC, likely a result of lower prescribed cohesive fracture strength and greater elastic anisotropy in the former. In both materials, the predicted Weibull modulus tends to decrease with an increasing number of grains contained in the simulated microstructure.

Published by Elsevier Ltd.

1. Introduction

Ceramic materials typically exhibit high hardness, high elastic stiffness, and low ductility relative to other engineering materials such as metals. Of interest in the present paper is the behavior of polycrystalline ceramics at conditions pertinent to ballistic impact: high loading rates (e.g., strain rates on the order of $10^5/s$) and high pressures (e.g., up to several to tens of GPa). The mechanical response of a polycrystalline ceramic under such conditions is dictated by bulk properties of its crystal constituents (e.g., density and elastic coefficients) as well as fracture behavior. Depending on the particular ceramic and loading regime, fracture can be transgranular and/or intergranular. Interactions among fractured and fragmented grains are thought to strongly affect shear strength behavior of damaged ceramics (Shockey et al., 1990; Curran et al., 1993; Gailly and Espinosa, 2002). Under severe loading, complete pulverization may occur; the comminuted ceramic may exhibit behavior approaching that of its powder form (Shih et al., 1998).

A general consensus on correlation between mechanical properties of ceramics and dynamic performance in high rate applications (e.g., resistance to failure, penetration, or perforation) apparently does not exist; relative importance of various properties may depend on the particular application. However, experiments do suggest that certain properties can strongly affect

dynamic performance. These properties include hardness, elastic stiffness, fracture toughness, unconfined compressive strength, dynamic shear strength, and failure probabilities (e.g., Weibull parameters) (Sternberg, 1989; Shockey et al., 1990; Curran et al., 1993; Gailly and Espinosa, 2002; Ray et al., 2007; Leavy et al., 2010). Experiments indicate that ceramics exhibit an increase in shear strength with increasing compressive pressure or confinement (Heard and Cline, 1980; Chen and Ravichandran, 2000). After fractures occur, dilatation accompanies sliding of mismatched or misaligned crack faces relative to one another. Increasing pressure resists this dilatation, increasing the amount of shear stress required to enable deviatoric deformation (Curran et al., 1993). This phenomena, which also occurs in rocks and minerals, can be interpreted in the context of Mohr–Coulomb or frictional sliding models (Chen and Ravichandran, 2000; Clayton, 2010a).

Efforts towards computational modeling of macroscopic behavior of polycrystalline ceramics under high strain rates and pressures representative of ballistic events have been underway for over three decades (Wilkins, 1978; Curran et al., 1993). More recently, mesoscale models, in which the behavior of each grain within a polycrystal is addressed explicitly, have provided insight into effects of microstructural properties – e.g., grain sizes and shapes, anisotropic elasticity and/or plasticity, local fracture properties, and distributions of second phases – on deformation and failure behavior of polycrystalline solids (Espinosa and Zavattieri, 2003a,b; Clayton and McDowell, 2004; Clayton, 2005a,b, 2006a,b; Vogler and Clayton, 2008; Foulk and Vogler, 2010; Kraft and

^{*} Corresponding author. Tel.: +1 410 2786146; fax: +1 410 2782460.

E-mail address: john.d.clayton1@us.army.mil (J.D. Clayton).

Molinari, 2008; Kraft et al., 2008; Zhang et al., 2005b,a; Kraft et al., 2010; Gazonas et al., 2010). Much earlier work focused on two-dimensional simulations; however, recent advances in computational hardware (e.g., processor speed and numbers of parallel processors), finite element software (Jung, 2010), and microstructure rendering and meshing technologies (Rollett and Manohar, 2004; Rollett et al., 2007) now enable fully resolved simulations of three-dimensional polycrystalline microstructures incorporating nonlinear material behavior, interfacial fracture, and multi-body contact (Kraft et al., 2010; Gazonas et al., 2010).

Three-dimensional simulations of polycrystalline microstructures are presented in this paper. Specific ceramics under consideration include silicon carbide (6H polytype as most prevalent in SiC-N, hexagonal structure) and AlON (spinel, cubic structure). Detailed descriptions and continuum models of behavior of single crystals of each material with supporting references are given elsewhere (Clayton, 2010c, 2011a). Notably, polycrystalline AlON of adequate quality is transparent, while polycrystalline SiC is opaque. However, SiC typically exhibits a higher elastic stiffness, higher fracture strength, and higher fracture toughness than AlON. Two synthetic microstructures are considered: one consisting of 50 grains, the other consisting of 126 grains. As discussed in more detail later, these microstructures are idealized in the sense that they do not correspond to reconstructions of actual specimens of the ceramics under present consideration; rather, they are synthesized from numerical algorithms incorporating grain growth or Voronoi methods. Synthetic microstructures of this sort are typically used when digital reconstructions of actual microstructures are not available (Zhang et al., 2005b; Clayton, 2009b; Foulk and Vogler, 2010). Properties of SiC or AlON are assigned to each microstructure in different simulations, and results of various simulations enable comparison between materials holding grain morphology fixed. Nonlinear anisotropic elasticity represents single crystals within each polycrystal. Intergranular fracture is addressed via a multi-body contact algorithm (Jung, 2010), whereby each grain is treated as a distinct solid body. The contact algorithm incorporates a cohesive law enabling tensile and shear fracture and accounting for fracture strength and surface energy of separation. Various initial lattice orientation distributions enable a study of effects of elastic anisotropy, while various loading directions (e.g., shear or compression along different axes) provide insight into effects of grain morphology and enable quantification of anisotropy of failure behavior.

Simulations consider the following boundary conditions: uniaxial strain compression, uniaxial stress compression, and shear with varying magnitudes of superimposed compressive pressure. All simulations are conducted at high loading rates ($10^5/s$). Uniform strain rates are assigned throughout each microstructure as an initial condition. Results from uniaxial strain and stress simulations are compared with available experimental data. However, the present simulations enable a study of specimens of sizes smaller (in terms of number of grains) than those accessible by standard high-rate experiments (e.g., traditional plate impact and Kolsky bar tests). Shear boundary conditions considered here do not correspond to known dynamic experiments on the materials of present interest and hence provide new insight into dynamic shear strength behavior, with and without pressure. Of particular interest in the present study are the following physical phenomena: dependence of dynamic shear strength on pressure, sensitivity of peak strength to grain morphology and elastic anisotropy, and dependence of statistical variations in peak strength on specimen size (i.e., number of grains) and local material properties. Pressure-dependent strength statistics from mesoscale simulations can be used to provide parameters entering macroscopic constitutive models for ceramic material behavior incorporating statistical

failure criteria (Brannon et al., 2007, 2009; Leavy et al., 2010; Graham-Brady, 2010).

This paper is structured as follows. Models for elastic behavior of single crystals, fracture of interfaces, and requisite material properties are described in Section 2. Microstructural representations (e.g., finite element meshes) are described in Section 3. Numerical simulations, important results, and limitations of the modeling approach are described in Section 4. Conclusions follow in Section 5.

Notation of continuum mechanics is used, primarily following index notation for vectors and higher-order tensors which is convenient in the context of anisotropic elasticity. Background on the subject of nonlinear anisotropic elasticity of crystals can be found in several books/monographs (Wallace, 1972; Thurston, 1974; Clayton, 2011b). For simplicity of presentation, all components of vectors and tensors are referred to a fixed set of Cartesian indices in both reference and spatial configurations of the body. Indices corresponding to the reference configuration are written in capitals, while those corresponding to the spatial configuration are written in lower case. Einstein's summation applies for repeated indices, e.g., $a_A b_A = a_1 b_1 + a_2 b_2 + a_3 b_3$.

2. Theory and constitutive models

Governing equations for elastic behavior of single crystals comprising polycrystalline aggregates are provided. Models for intergranular fracture are described. Properties for bulk single crystals and interfaces are tabulated for SiC and AlON ceramics.

2.1. Nonlinear anisotropic elasticity

The behavior of intact single crystals is governed by traditional balance laws of nonlinear continuum mechanics (Thurston, 1974; Clayton, 2011b). Letting t denote time, spatial (x_a) and material (X_A) coordinates are related by the smooth, invertible, and one-to-one (at any given time) functions

$$x_a = x_a(X_A, t), \quad X_A = X_A(x_a, t). \quad (1)$$

The deformation gradient and its inverse are

$$F_{aA} = \partial x_a / \partial X_A = \partial_A x_a, \quad F_{Aa}^{-1} = \partial X_A / \partial x_a = \partial_a X_A, \quad (2)$$

where partial coordinate differentiation (t fixed) obeys

$$\partial_A(\cdot) = \partial(\cdot) / \partial X_A = [\partial(\cdot) / \partial x_a] [\partial x_a / \partial X_A] = \partial_a(\cdot) F_{aA}. \quad (3)$$

Volume element dV in the spatial configuration is related to its counterpart dV_0 in the reference configuration by the Jacobian determinant J :

$$J = dV / dV_0 = \det(F_{aA}) = \frac{1}{6} \epsilon_{abc} \epsilon_{ABC} F_{aA} F_{bB} F_{cC} \quad (4)$$

with inverse

$$J^{-1} = 1/J = \det(F_{Aa}^{-1}) = \frac{1}{6} \epsilon_{abc} \epsilon_{ABC} F_{Aa}^{-1} F_{Bb}^{-1} F_{Cc}^{-1}. \quad (5)$$

Permutation symbols are ϵ_{abc} and ϵ_{ABC} . The following identities apply (Clayton, 2011b):

$$\begin{aligned} \partial J / \partial F_{aA} &= J F_{Aa}^{-1}, & \partial_A (J F_{Aa}^{-1}) &= 0; \\ \partial J^{-1} / \partial F_{Aa}^{-1} &= J^{-1} F_{aA}, & \partial_a (J^{-1} F_{aA}) &= 0. \end{aligned} \quad (6)$$

Let the following notations denote the material time derivative:

$$d(\cdot) / dt = (\cdot) = [\partial(\cdot) / \partial t]_{X_A} = [\partial(\cdot) / \partial t]_{x_a} + v_a \partial_a(\cdot). \quad (7)$$

Particle velocity and acceleration, respectively, are

$$v_a = \dot{x}_a, \quad a_a = \dot{v}_a = \ddot{x}_a. \quad (8)$$

The spatial velocity gradient and its trace obey

$$\partial_b v_a = \dot{F}_{aA} F_{Ab}^{-1}, \quad \partial_a v_a = j \dot{J}^{-1}. \quad (9)$$

Cauchy stress σ_{ab} , first Piola–Kirchhoff stress P_{aA} , and second Piola–Kirchhoff stress S_{AB} are related by

$$\sigma_{ab} = J^{-1} P_{aB} F_{bB} = J^{-1} F_{aA} S_{AB} F_{bB}. \quad (10)$$

Conservation laws for mass, linear momentum (with no body forces), and angular momentum are

$$\rho_0 = \rho J, \quad \partial_A P_{aA} = \rho_0 a_a, \quad P_{aB} F_{bB} = P_{bB} F_{aB}, \quad (11)$$

where ρ_0 and ρ are referential and spatial mass densities. Using (6), (9), and (10),

$$\dot{\rho} = -\rho \partial_a v_a, \quad \partial_b \sigma_{ab} = \rho a_a, \quad \sigma_{ab} = \sigma_{ba}. \quad (12)$$

Assuming adiabatic conditions, the balance of energy and entropy inequality are

$$\dot{U} = P_{aA} \dot{F}_{aA}, \quad \dot{\eta} \geq 0, \quad (13)$$

where U and η are entropy and internal energy per unit reference volume.

A hyperelastic material response is assumed:

$$U = U(F_{aA}, \eta), \quad \partial U / \partial F_{aA} = P_{aA}, \quad \partial U / \partial \eta = \theta, \quad (14)$$

with θ the temperature. From the chain rule and (14),

$$\dot{U} = P_{aA} \dot{F}_{aA} + \theta \dot{\eta}, \quad (15)$$

which is compatible with adiabatic assumption (13) at finite temperature only when $\dot{\eta} = 0$; i.e., assumptions of adiabatic conditions and hyperelastic response correspond to isentropic conditions. Thus, dependence of internal energy on entropy is dropped henceforward, and thermomechanical quantities are assumed to be measured at fixed entropy (e.g., the usual “adiabatic” elastic coefficients measured ultrasonically).

Define symmetric Lagrangian elastic strain E_{AB} and deformation C_{AB} as

$$E_{AB} = \frac{1}{2} (C_{AB} - \delta_{AB}), \quad C_{AB} = F_{aA} F_{aB}, \quad \det(C_{AB}) = J^2, \quad (16)$$

with δ_{AB} Kronecker's delta. The internal energy at fixed entropy is, to within an arbitrary constant and to third order in strain (Thurston, 1974; Clayton, 2011b),

$$U = \frac{1}{2!} \frac{\partial^2 U}{\partial E_{AB} \partial E_{CD}} \bigg|_{E_{ij}=0} E_{AB} E_{CD} + \frac{1}{3!} \frac{\partial^3 U}{\partial E_{AB} \partial E_{CD} \partial E_{EF}} \bigg|_{E_{ij}=0} E_{AB} E_{CD} E_{EF} \\ = \frac{1}{2} C_{ABCD} E_{AB} E_{CD} + \frac{1}{6} C_{ABCDEF} E_{AB} E_{CD} E_{EF}. \quad (17)$$

Second- and third-order elastic constants at the unstressed reference state are C_{ABCD} and C_{ABCDEF} . In Voigt's notation (Thurston, 1974; Clayton, 2011b), where Greek indices run from 1 to 6, $C_{ABCD} \leftrightarrow C_{\alpha\beta}$ and $C_{ABCDEF} \leftrightarrow C_{\alpha\beta\gamma}$. Noting from (10) and the symmetry of E_{AB} and S_{AB} that

$$P_{aA} = \partial U / \partial F_{aA} = (\partial U / \partial E_{BC}) (\partial E_{BC} / \partial F_{aA}) = (\partial U / \partial E_{BA}) F_{aB} = F_{aB} S_{BA}, \quad (18)$$

it follows that the second Piola–Kirchhoff stress

$$S_{AB} = C_{ABCD} E_{CD} + \frac{1}{2} C_{ABCDEF} E_{CD} E_{EF}. \quad (19)$$

Properties for SiC and AlON single crystals are listed in Table 1. Third-order elastic constants are tedious to measure and have been reported for relatively few substances. For many single crystals, including those of interest here, full sets of third-order elastic constants have not been reported in the literature. However, third-order elastic constants can be estimated as follows (Clayton, 2010c, 2011a), presuming pressure derivatives of elastic coefficients at the reference state are available. First, note the following identity (Clayton, 2011b):

$$\partial J / \partial E_{AB} = 2 \partial J / \partial C_{AB} = J^{-1} (\partial J^2) / \partial C_{AB} = J^{-1} \partial \det(C_{AB}) / \partial C_{AB} \\ = J^{-1} \det(C_{AB}) C_{BA}^{-1} = J C_{AB}^{-1}. \quad (20)$$

Now, assume that the tangent elastic coefficients (denoted with a superposed \wedge) depend only on volume change (via J) and not on deviatoric deformation:

$$\hat{C}_{ABCD}(J) = \partial^2 U / \partial E_{AB} \partial E_{CD}. \quad (21)$$

Using (20), and letting $\hat{K} = -V(dp/dV) = -J(dp/dJ)$ denote the tangent bulk modulus with $p = -\sigma_{aa}/3$ the Cauchy pressure,

$$\partial \hat{C}_{ABCD} / \partial E_{EF} = (d\hat{C}_{ABCD} / dJ) (\partial J / \partial E_{EF}) \\ = (d\hat{C}_{ABCD} / dp) (dp / dJ) (\partial J / \partial E_{EF}) \\ = -(d\hat{C}_{ABCD} / dp) (\hat{K} / J) (J C_{EF}^{-1}) \\ = -\hat{K} (d\hat{C}_{ABCD} / dp) C_{EF}^{-1}. \quad (22)$$

Table 1
Properties for SiC and AlON single crystals.

Property	Value (SiC)	Reference	Value (AlON)	Reference
Structure	6H polytype		Spinel	
Phase	α		γ	
Crystal system	Hexagonal		Cubic	
Mass density ρ_0	3227 kg/m ³	Leavy et al. (2010)	3714 kg/m ³	Graham et al. (1988)
Elastic constant C_{11}	501 GPa	Kamitani et al. (1997)	301 GPa	Gazonas et al. (2010)
Elastic constant C_{12}	112 GPa		155 GPa	
Elastic constant C_{44}	161 GPa		174 GPa	
Elastic constant C_{13}	52 GPa		(= C_{12})	
Elastic constant C_{33}	549 GPa		(= C_{11})	
Pressure derivative dC_{11}/dp	3.8	Davydov (2004)	5.1	Batyrev et al. (2011)
Pressure derivative dC_{12}/dp	4.0		2.7	
Pressure derivative dC_{44}/dp	−0.2		1.2	
Pressure derivative dC_{13}/dp	4.0		(= dC_{12}/dp)	
Pressure derivative dC_{33}/dp	3.8		(= dC_{11}/dp)	
No. independent $C_{\alpha\beta\gamma}$	10		6	
Bulk modulus K	222 GPa	Clayton (2010c)	204 GPa	($C_{11} + 2C_{12}$)/3
Shear modulus G	194 GPa		134 GPa	(Voigt average)
Poisson's ratio ν	0.16		0.23	
Shear wave speed $\sqrt{G/\rho_0}$	7.75 km/s		6.01 km/s	
Zener anisotropy $2C_{44}/(C_{11} - C_{12})$	0.83		2.38	
Typical grain size	5 μ m	Leavy et al. (2010)	200 μ m	McCauley et al. (2009)

Repeating (22) over alternating pairs of indices (AB, CD, EF), evaluating at the reference state where $C_{AB}^{-1} = \delta_{AB}$, $dC_{ABCD}/dJ = dC_{ABCD}/dJ$, $\hat{K} = K$ (i.e., dropping the \wedge notation at the reference state) and averaging the result provides the following estimate of third-order elastic constants with requisite major and minor symmetries:

$$C_{ABCDEF} \approx -(K/3)[(dC_{ABCD}/dp)\delta_{EF} + (dC_{CDEF}/dp)\delta_{AB} + (dC_{EFAB}/dp)\delta_{CD}]. \quad (23)$$

Application of (23) to single crystals of alumina (Al_2O_3), a material for which $\partial C_{\alpha\beta}/\partial p$ and $C_{\alpha\beta\gamma}$ are known (Hankey and Schuele, 1970; Clayton, 2009a, 2010b) provides a coarse yet reasonable estimate of 11 of its 14 third-order elastic constants. Application of (23) to single crystals of SiC provides an accurate depiction of the hydrostat (Clayton, 2010c). As demonstrated in previous modeling efforts for SiC (Clayton, 2010c) and AlON (Clayton, 2011a), third-order elastic constants enable description of the increase in tangent elastic stiffness that accompanies decreasing volume. The exact relationship (Thurston et al., 1966) $\partial C_{ABCD}/\partial p = -S_{EFGG}C_{ABCDEF}$, with S_{ABCD} the compliance, provides an insufficient number of equations for determination of all third-order constants.

2.2. Fracture

A cohesive zone approach is used to model intergranular fracture. Let t_a^n and t_a^t denote traction vector components normal and tangential to a potential fracture site with unit outward normal components n_a :

$$t_a^n = (\sigma_{bc}n_b n_c)n_a, \quad t_a^t = \sigma_{ab}n_b - (\sigma_{bc}n_b n_c)n_a; \quad |t_a^n| = \sqrt{t_a^n t_a^n}, \quad |t_a^t| = \sqrt{t_a^t t_a^t}. \quad (24)$$

Many cohesive laws have been investigated in previous works on heterogeneous polycrystalline solids (Espinosa and Zavattieri, 2003a,b; Clayton and McDowell, 2004; Clayton, 2005a,b; Kraft and Molinari, 2008; Kraft et al., 2008; Vogler and Clayton, 2008; Foulk and Vogler, 2010; Kraft et al., 2010). A simple irreversible cohesive law is prescribed in the present work, with the same functional form and parameters for normal and tangential separations δ^n and δ^t . Specifically, separation is possible after a critical initiation traction of magnitude t^c is attained. The interface then maintains a constant cohesive strength until critical separation distance δ^c is reached. Mathematically,

$$\delta^n = 0 \leftrightarrow |t_a^n| < t^c, \quad 0 < \delta^n / \delta^c < 1 \leftrightarrow |t_a^n| = t^c, \quad \delta^n / \delta^c \geq 1 \leftrightarrow |t_a^n| = 0; \\ \delta^t = 0 \leftrightarrow |t_a^t| < t^c, \quad 0 < \delta^t / \delta^c < 1 \leftrightarrow |t_a^t| = t^c, \quad \delta^t / \delta^c \geq 1 \leftrightarrow |t_a^t| = 0. \quad (25)$$

Normal separation only occurs for tensile normal stress, i.e., for $t_a^n n_a > 0$; interpenetration of matter is prohibited. After complete separation, interactions between interfaces are addressed via a multi-body contact algorithm (Jung, 2010) enabling sliding between faces but no interpenetration. Atomic bonds are considered irreversibly broken when either δ^n or δ^t exceeds δ^c ; i.e., once complete fracture occurs in any direction at a given referential location, cohesive strength is lost in all directions at that location. The advantage of cohesive law (25) is its simplicity: only two parameters, which can be estimated from macroscopic fracture measurements, are needed. Coupling does not exist between normal and tangential contributions to fracture energy in later Eq. (26); surface energy Γ is the same for pure normal or pure tangential fracture, but the total surface energy associated with an interface undergoing mixed mode fracture may exceed Γ . As discussed later in Section 4, (25) produces an adequate representation of macroscopic stress-strain and failure behaviors of ceramic polycrystals under present consideration. More complex cohesive laws incorporating

piecewise-linear traction-separation relationships with various slopes were investigated; alternative formulations did not offer any apparent advantages with regards to numerical stability or representation of macroscopic fracture strength but often would require specification of experimentally unknown parameters.

Differently from many previous studies (Espinosa and Zavattieri, 2003a,b; Clayton and McDowell, 2004; Clayton, 2005a,b; Vogler and Clayton, 2008; Foulk and Vogler, 2010), distinct cohesive finite elements are not used in the present numerical framework. In other words, finite element meshes are not seeded a priori with interfacial elements. Rather, the cohesive constitutive law (25) is incorporated directly into the contact algorithm (Jung, 2010), and each individual grain within a polycrystalline aggregate is treated as a distinct solid body from the outset of a given numerical simulation. Prior to attainment of the critical normal or tangential traction, interfaces are rigidly tied, and hence artificial increases in compliance prior to fracture initiation are avoided. Once the critical traction is attained and separation commences, forces resulting from the cohesive traction-separation law are effectively applied to appropriate nodes by the contact algorithm that computes node-face interactions (Jung, 2010, Ch. 7, pp. 377–448).

Properties are listed for SiC and AlON in Table 2, with critical strength and separation distance computed using experimental (macroscopic) values of flexure strength and static fracture toughness. In the context of linear elastic fracture mechanics, fracture toughness κ , surface energy Γ , critical strength t^c , critical separation δ^c , and cohesive zone length l^c are related by (Espinosa and Zavattieri, 2003b; Clayton, 2005b; Kraft et al., 2010)

$$\kappa^2(1 - \nu^2)/E = 2\Gamma = t^c \delta^c, \quad l^c \approx \pi E \Gamma / [(t^c)^2(1 - \nu^2)]. \quad (26)$$

Young's modulus $E = 9KG/(3K + G)$ and Poisson's ratio $\nu = (3K - 2G)/(6K + 2G)$. Also shown for purposes of comparison in Table 2 are experimentally measured spall strengths. Spall strengths are comparable to flexure strengths, though the former may vary considerably with impact pressure (Dandekar and Bartowski, 2001; Cazamias et al., 2001) and may also vary from sample to sample tested at similar impact pressures due to brittleness and possible flaws in the material.

The present study incorporates uniform grain boundary strength and frictionless post-fracture sliding between grain boundary facets. It is understood that real ceramic microstructures should exhibit variation among fracture behaviors (e.g., in functional forms of cohesive laws as well as in fracture strengths and energies) at interfaces depending on grain misorientation, grain boundary curvature, impurities, and pre-existing defects. Thus, the assumption of uniform grain boundary behavior is an idealization, albeit one that has been used frequently in other numerical studies of heterogeneous polycrystalline solids (Clayton and McDowell, 2004; Vogler and Clayton, 2008; Foulk and Vogler, 2010; Kraft et al., 2010). Variable grain boundary properties can strongly influence overall behavior of ceramics (Espinosa and Zavattieri, 2003b; Kraft and Molinari, 2008; Kraft et al., 2008); however, assignment of variable properties as an initial condition is problematic since experimental measurements of mesoscopic grain boundary strength distributions are scarce if not nonexistent. A distribution of strengths at the mesoscale could be assigned so that homogenized model results over many simulations would match macroscopic failure statistics (e.g., a Weibull modulus). However, such an approach would reduce model calculations of failure statistics to parameter fits rather than predictive results. On the other hand, assignment of uniform grain boundary properties enables simulation results to provide insight of other sources of variability, such as grain morphology, loading conditions, and elastic anisotropy, on predicted failure statistics.

Table 2
Properties for SiC and AlON interfaces.

Property	Value (SiC)	Reference	Value (AlON)	Reference
Fracture (flexure) strength σ^c	0.570 GPa	Leavy et al. (2010), LaSalvia et al. (2010)	0.306 GPa	Corbin (1989)
Fracture toughness K	5.1 MPa m ^{1/2}		2.5 MPa m ^{1/2}	
Surface energy Γ	28.1 J/m ²	Eq. (26)	9.0 J/m ²	Eq. (26)
Critical separation δ^c	0.10 μ m		0.06 μ m	
Cohesive length l^c	126 μ m		105 μ m	
Spall strength	0.54–1.3 GPa	Dandekar and Bartowski (2001)	0.14–1.7 GPa	Cazamias et al. (2001)

The assumption of local frictionless contact enables smooth faces to slide freely past one another. However, as will be demonstrated later in Section 4, because grain boundaries are interlocking, grains cannot slide indefinitely without expansion normal to the direction of motion and generation of free volume, i.e., dilatation (Curran et al., 1993; Clayton, 2010a). This phenomenon, due simply to grain geometry, leads to an increase in macroscopic or average shear stress with confinement or compressive pressure, in what may be interpreted as sliding “friction” in the sense of macroscopic Mohr–Coulomb models (Chen and Ravichandran, 2000), even though microscopically contact is treated as frictionless. Locally frictionless contact was also assumed in a previous computational study of shock compression and spall of SiC (Foulk and Vogler, 2010). However, this approach represents a limiting case since local microscopic friction could be non-negligible. Previous two dimensional simulations (Kraft et al., 2008) demonstrated that as the sliding friction coefficient between failed grain boundaries increases, compressive peak strength and its sensitivity to confining stress also increase. As noted later in Section 4.4, omission of friction may contribute to under-prediction of shear strength in the present simulations of the high pressure response under uniaxial strain loading, wherein contributions of frictional forces proportional to normal pressures at interfaces could become important.

As assumed in previous fracture simulations of ceramic polycrystals including Al₂O₃ (Espinosa and Zavattieri, 2003a; Espinosa and Zavattieri, 2003b), SiC (Foulk and Vogler, 2010), and AlON (Gazonas et al., 2010), transgranular (i.e., cleavage) fracture is not addressed. This is a reasonable assumption for certain varieties of SiC (e.g., SiC-N) that contain additives that segregate at grain boundaries, leading to a tendency for grain boundary fracture over cleavage and corresponding to increased toughness (Faber and Evans, 1983; Shih et al., 1998; Lee et al., 2005; Vargas-Gonzalez et al., 2010). On the other hand, this assumption may be less physically reasonable for AlON, in which cleavage fractures have been observed (McCauley et al., 2009).

3. Microstructure modeling

Synthetic microstructures representative of generic polycrystals with equi-axed grains are considered in the present work, in the absence of serial section and/or electron back-scatter diffraction (EBSD) data that could be used to recreate true microstructures from material specimens (Brahme et al., 2006; Rollett et al., 2007). Efforts are presently underway towards reconstruction of microstructures from actual ceramic specimens. In the present approach, volume meshes (tetrahedral elements) are created from stereolithographic (STL) files of surface representations of grains comprising a given microstructure. Surface meshes are generated for three-dimensional microstructures produced using a Monte Carlo grain growth algorithm (Rollett and Manohar, 2004). A conformal triangular surface mesh covers each crystal volume, with an interpolation method used where a triangle separates two materials (Kraft et al., 2010). A three dimensional volume mesh of tetra-

hedral continuum finite elements is then created to fill the surface mesh of every crystal.

Two microstructures are considered: microstructure I, with 50 grains; and microstructure II, with 126 grains. Each aggregate is a cube of dimensions $L \times L \times L$, where $L = 1$ mm. Absolute dimensions of each aggregate are prescribed to be equal to enable reasonable comparison of dynamic finite element results between microstructures in which traction-free boundary conditions are prescribed on some external surfaces. If, on the other hand, different sized specimens were to be compared, differences in deformation and failure behavior could, in many scenarios, be attributed to differences in dimensions of external boundaries of the aggregate. For example, a planar crack originating at one edge of the aggregate would propagate (at constant speed) in a shorter time across a smaller specimen than a larger specimen, leading to earlier failure in the former case. Times for elastic release waves to traverse different-sized specimens would also differ in dynamic simulations. By using the same absolute size L for each aggregate, any such issues associated with external boundaries are the same in each simulation, so that results obtained from different microstructures can be meaningfully compared. As discussed later in Section 4.3, periodic boundary conditions might be expected to provide more realistic depiction of behavior of grain aggregates embedded inside a much larger sample of material, as considered elsewhere in two-dimensional studies of ceramic microstructures (Espinosa and Zavattieri, 2003a,b).

Microstructures are shown in Fig. 1. Average grain sizes for each microstructure can be estimated as $L/50^{1/3} \approx 270 \mu\text{m}$ (microstructure I) and $L/126^{1/3} \approx 200 \mu\text{m}$ (microstructure II), which are representative of AlON (McCauley et al., 2009) but are much larger than standard SiC-N (Lee et al., 2005; Leavy et al., 2010). However, other varieties of polycrystalline SiC with large grains can exhibit grain sizes of this order of magnitude (Rice et al., 1994). As mentioned in Section 1, the same microstructures are used to represent both SiC and AlON polycrystals in subsequent dynamic finite element simulations. Use of the same meshes for each material enables quantification of differences in deformation and failure behavior by varying material properties (i.e., mass density, elasticity, cohesive strength, and cohesive energy) while holding the microstructure fixed. Differences resulting from grain morphology are studied by compressing and/or shearing each microstructure in different (e.g., orthogonal and forward/reverse) directions. Finite element meshes contain between 1×10^6 and 2×10^6 tetrahedral elements. Mesh refinement is sufficient to resolve grain boundary surface morphology and cohesive zone lengths (Table 2) and is comparable to that considered in previous polycrystal fracture simulations in two and three dimensions (Clayton, 2005a,b; Kraft and Molinari, 2008; Kraft et al., 2008, 2010; Gazonas et al., 2010). Cumulative grain size distributions for each microstructure are shown in Fig. 2. Let V_g denote the volume V of a particular grain, and define that grain's size as $V_g^{1/3}$. The cumulative number fraction (ordinate of Fig. 2) is defined as the number of grains with $V_g^{1/3} \leq V^{1/3}$ divided by the total number of grains in the microstructure. The abscissa of Fig. 2 is $V^{1/3}$ normalized by the average grain size in the microstructure. Grain sizes are somewhat more uniform

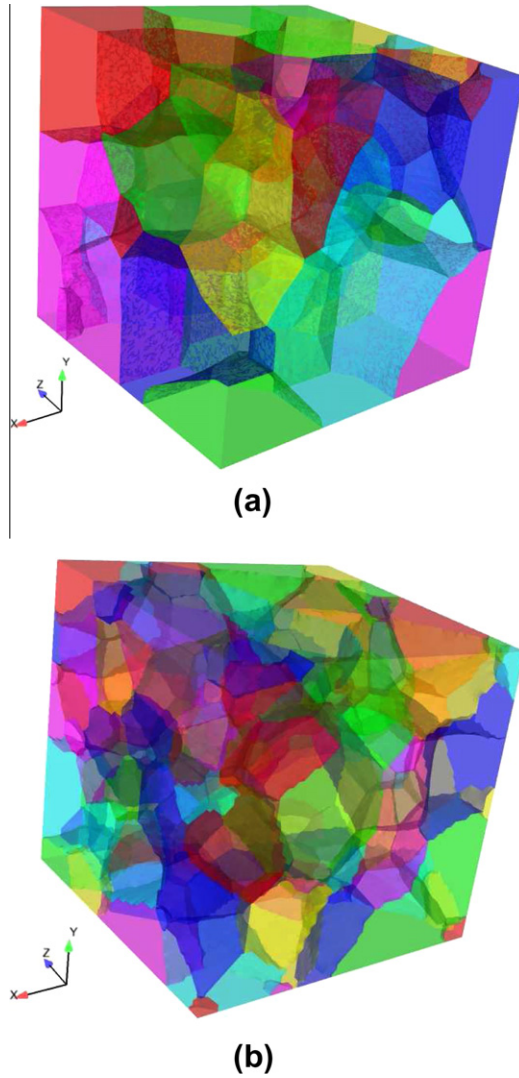


Fig. 1. Finite element representations of polycrystalline aggregates: (a) microstructure I (50 grains) (b) microstructure II (126 grains).

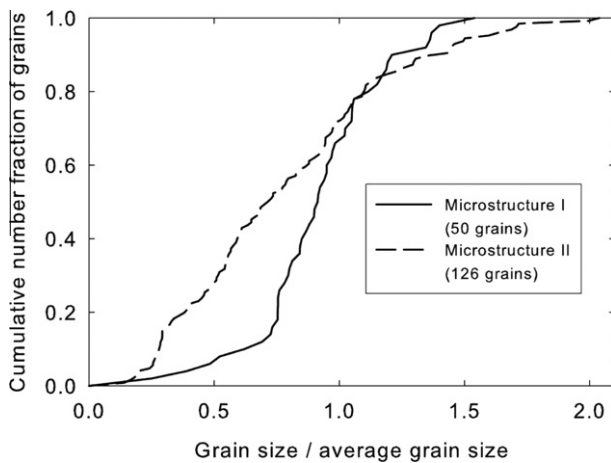


Fig. 2. Normalized cumulative grain size distributions.

in microstructure I, while microstructure II exhibits greater variability (i.e., a wider distribution) of grain sizes. Normalized distributions are qualitatively similar to those observed for Hexoloy SiC and SiC-N (Vargas-Gonzalez et al., 2010).

In all simulations discussed in Section 4, random initial lattice orientations are used for grains comprising each microstructure. Different sets of random initial orientations are investigated in some simulations. Lattice orientation affects model results through the dependence of anisotropic elastic coefficients (C_{ABCD} , C_{ABCDEF}) on crystallographic orientation in the reference configuration.

4. Mesoscale simulations

Dynamic simulations for different boundary and initial conditions are described in what follows: uniaxial strain compression (Section 4.1), uniaxial stress compression (Section 4.2), and shear (Section 4.3) with and without superimposed compressive stress. Results are then summarized in Section 4.4, with limitations of the current approach and areas for further research identified.

Data from numerous mesoscale simulations are collected and analyzed, approximately 180 simulations in total. The SIERRA (Jung, 2010) Lagrangian finite element code with explicit dynamics is used. Each simulation is executed in parallel mode on 32 processors for 24 h wall-clock time, for a total number of cpu-hours consumed of $180 \times 32 \times 24 \approx 1.4 \times 10^5$.

4.1. Uniaxial strain

Results for dynamic uniaxial strain loading are reported first. Let X denote the referential direction of loading, with Y and Z denoting orthogonal directions, and with a corner of the cubic specimen located initially at the origin $(X, Y, Z) = (0, 0, 0)$. Velocity boundary conditions and nonzero initial conditions for uniaxial straining in the X -direction are, respectively,

$$\begin{aligned} v_x &= -\dot{\epsilon}X \quad \text{along } X = L; \\ v_y &= 0 \quad \text{along } Y = 0, L; \\ v_z &= 0 \quad \text{along } Z = 0, L; \end{aligned} \quad (27)$$

$$v_x = v_y = v_z = 0 \quad \text{along } X = 0;$$

$$v_x(t=0) = -\dot{\epsilon}X \leftrightarrow \partial_x v_x(t=0) = -\dot{\epsilon}. \quad (28)$$

The imposed uniaxial strain rate is $\dot{\epsilon} = 10^5/\text{s}$. Initial conditions (28) impose a uniform initial velocity gradient throughout the domain; a shock wave would arise, on the other hand, if velocity boundary conditions (27) were to be applied to a body initially at rest. Uniaxial strain simulations were also performed via loading in orthogonal Y and Z directions, with analogous boundary and initial conditions. Under these loading conditions, volume V of the aggregate is related to its initial volume V_0 via $V = (1 - \dot{\epsilon}t)V_0$.

Because the material is unstrained at $t = 0$, stress is zero everywhere initially. The strain rate (symmetric part of the velocity gradient $\partial_b v_a$) is initially nonzero and constant throughout the microstructure. If these conditions were to be applied to a homogeneous linear elastic material, stresses would increase linearly with time. In the present simulations, stresses may emerge heterogeneously and nonlinearly with $t > 0$ as a result of elastic anisotropy and elastic nonlinearity, fracture, contact, and stress wave interactions. The authors are unaware of any experimental configuration that exactly replicates these uniform initial and boundary conditions. Similar comments apply for other initial and boundary conditions considered later in Section 4.2 and Section 4.3.

Fig. 3 shows axial stress contours ($\sigma = -\sigma_{xx}$, positive in compression) in SiC (Fig. 3(a)) and ALON (Fig. 3(b)). In each case shown, a 50-grain microstructure is deformed to 5% reduction in volume, i.e., $V/V_0 = 0.95$ via compression along the X -direction. Stresses are significantly higher in SiC than ALON as a result of the larger elastic stiffness and higher fracture strength and toughness in the former (Tables 1 and 2). In each microstructure, cracks associated with axial splitting appear, typical behavior for brittle materials

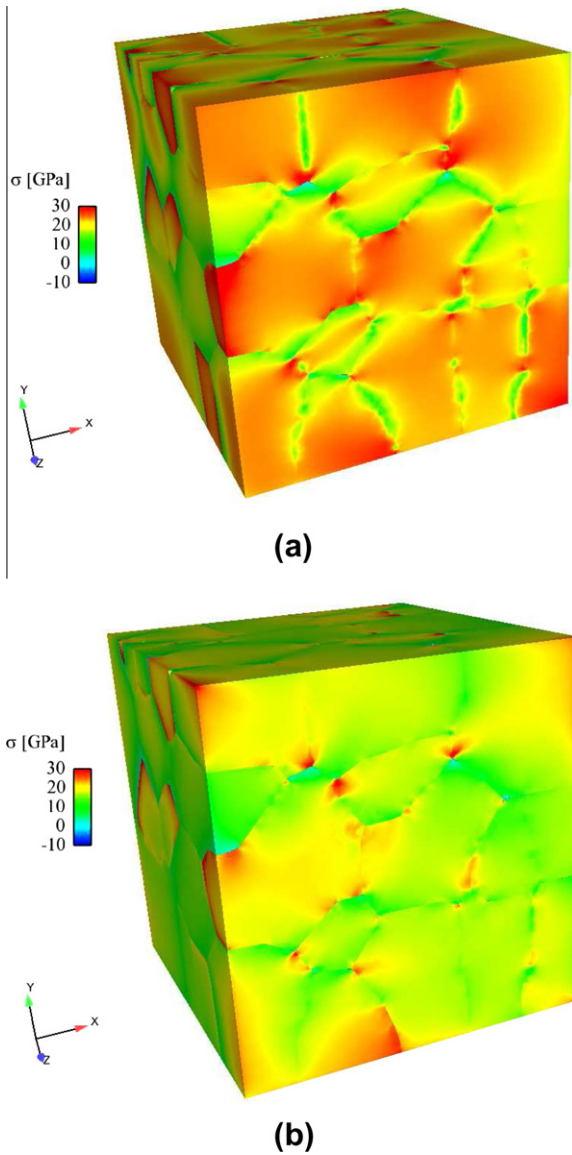


Fig. 3. Axial stress σ (positive in compression) for 50-grain microstructures subjected to uniaxial strain at volume $V/V_0 = 0.95$: (a) SiC (b) AlON.

with low Poisson's ratio (Chen and Ravichandran, 2000). Stress concentrations are visible along certain grain boundaries and triple junctions in both materials.

Average axial stress Σ is defined as the surface integral

$$\Sigma = (1/A) \int_A \hat{t}^n dA, \quad (29)$$

where \hat{t}^n is the magnitude of the component of traction normal to loaded surface A . For example, for uniaxial strain along the X -direction, $\hat{t}^n = |\sigma_{xx}n_x| = |\sigma_{xx}|$ along the surface defined by $X = L$ with area $A = L^2$. Average axial stresses are shown in Fig. 4(a) and (b) for respective microstructures of SiC and AlON loaded along the X -direction. Results are compared for specimens in which fracture is prohibited (i.e., permanently tied contact at grain boundary interfaces), for specimens with different random grain orientation distributions (labeled orientation 1 and orientation 2), and for nonlinear and linear elastic constitutive models. Nonlinear elastic models incorporating both second- and third-order elastic constants are used unless simulation cases are labeled as “linear”. For linear models, only anisotropic second-order elastic constants are implemented, and all third-order

elastic constants are set to zero. For each material, simulations without fracture exhibit the largest stiffness. Average stresses from simulations incorporating nonlinear elasticity with different lattice orientations are nearly indistinguishable in each of Fig. 4(a) and (b). Also in each material, differences between nonlinear and linear elastic models become apparent at larger compressions (e.g., at $V/V_0 \leq 0.97$). For the same material, lattice orientation, and grain geometry, nonlinear elasticity provides for a higher compressive stress than linear elasticity because of the increasing elastic stiffness with increasing compressive pressure reflected by the third-order elastic constants.

Average axial stresses for SiC and AlON microstructures with various lattice orientations strained uniaxially along different directions are compared to experimental shock compression data in Fig. 5(a) and (b). Note that uniaxial strain compression at a rate of $\dot{\epsilon} = 10^5/s$ is typically deemed representative of plate impact experiments (Grady, 1998; Clayton, 2011a), though the stress state is not uniform in shock compression tests. A uniaxial strain condition with a constant strain rate of $\dot{\epsilon} = 10^5/s$ was used elsewhere (Holmquist and Johnson, 2002) to calibrate a macroscopic ceramic strength model to plate impact data. Constitutive models used in the present work for nonlinear elasticity, cohesive fracture, and contact include no intrinsic rate dependence. Rate effects arise only from time scales associated with inertia (i.e., elastic wave speeds in anisotropic grains) and crack propagation velocities. Experimental data shown in Fig. 5 correspond to shock compression, wherein the strain rate and stress state exhibit effective jump discontinuities across the shock front. On the other hand, model results are obtained for the more homogeneous uniaxial strain loading path dictated by (27) and (28). Differences between model predictions and experimental data would be expected due to the path dependent nature of the fracture process, e.g., local fractures induced by propagation of a shock front are omitted in the simulations.

Predicted average stresses for SiC shown in Fig. 5(a) are very similar for all orientations and all loading directions. Except for the first experimental data point shown (which corresponds to the elastic regime), predicted stresses are lower than experimental plate impact data (Feng et al., 1998; Yuan et al., 2001). Possible reasons for discrepancies are discussed further in Section 4.4. Predicted average stresses for AlON shown in Fig. 5(b) are also very similar for all orientations and all loading directions. Furthermore, predictions for AlON closely follow the experimental plate impact data (Cazamias et al., 2001; Vaughan et al., 2001; Dandekar et al., 2007).

Tables 3 and 4 report average shear stresses for SiC and AlON, respectively. Simulation cases are tabulated in Table 5. Average shear stress τ and average pressure P follow the usual definitions from shock compression science (Feng et al., 1998; Grady, 1998; Dandekar et al., 2007; Clayton, 2011a,b):

$$\tau = \frac{1}{2}(\Sigma_1 - \Sigma_3), \quad P = -\frac{1}{3}(\Sigma_1 + \Sigma_2 + \Sigma_3), \quad (30)$$

where Σ_1, Σ_2 , and Σ_3 are maximum, intermediate, and minimum principal stresses for the polycrystalline aggregate computed analogously to (29). Shear stress increases monotonically with compressive strain in all simulations. In experiments on SiC (Feng et al., 1998), shear strength increases with increasing compressive strain for $V/V_0 \geq 0.95$, while in experiments on AlON (Dandekar et al., 2007), shear strength decreases for compressive strain $V/V_0 \leq 0.98$. Agreement between model and experiment is closer at larger compressions. Missing entries in Tables 3 and 4 indicate either unreported experimental data or simulations that were terminated due to numerical instabilities prior to attainment of corresponding applied strains. Slight variations in shear strength among simulations of the same material loaded in different directions or with different lattice orientations are evident, generally on the

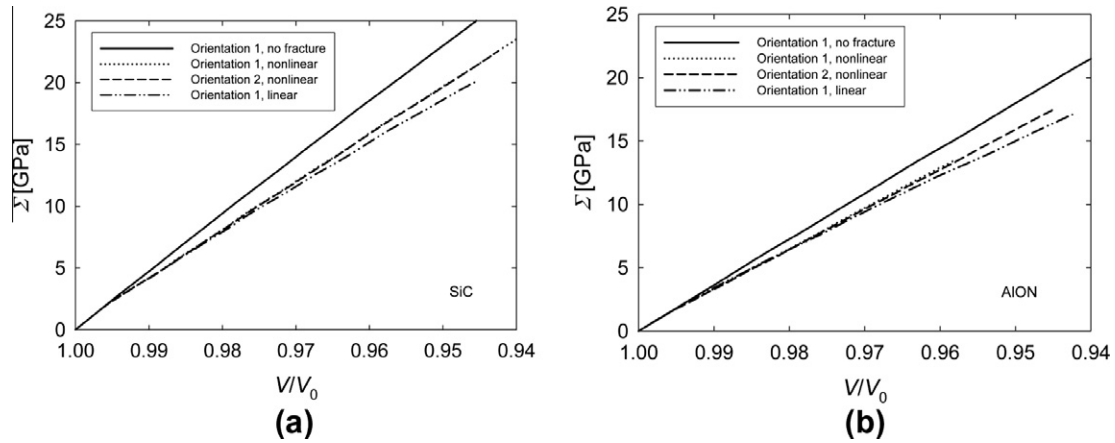


Fig. 4. Average axial stress Σ for the same microstructures subjected to uniaxial strain along X-direction: (a) SiC (b) AlON.

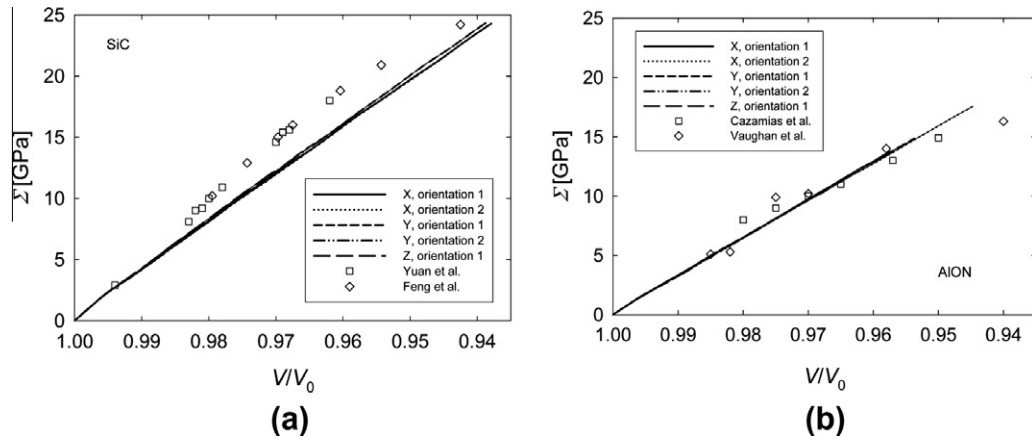


Fig. 5. Average axial stress Σ for the same grain structures subjected to uniaxial strain along different directions, and experimental shock compression data: (a) SiC (b) AlON.

Table 3

Predicted and experimental shear stress for SiC in uniaxial strain compression.

Simulation or experiment	τ [GPa]					
	$\frac{V}{V_0} = 0.99$	$\frac{V}{V_0} = 0.98$	$\frac{V}{V_0} = 0.97$	$\frac{V}{V_0} = 0.96$	$\frac{V}{V_0} = 0.95$	$\frac{V}{V_0} = 0.94$
Simulation 1	1.49	2.70	3.87	4.97	6.00	6.97
Simulation 2	1.46	2.65	3.77	4.86	5.86	–
Simulation 3	1.48	2.68	3.83	4.92	5.94	–
Simulation 4	1.51	2.78	4.04	5.15	6.31	7.29
Simulation 5	1.49	2.74	3.97	5.09	–	–
Simulation 6	1.53	2.84	4.17	–	–	–
Simulation 7	1.54	2.85	–	–	–	–
Experiment Feng et al. (1998)	–	4.18	5.80	6.85	6.95	6.90

Table 4

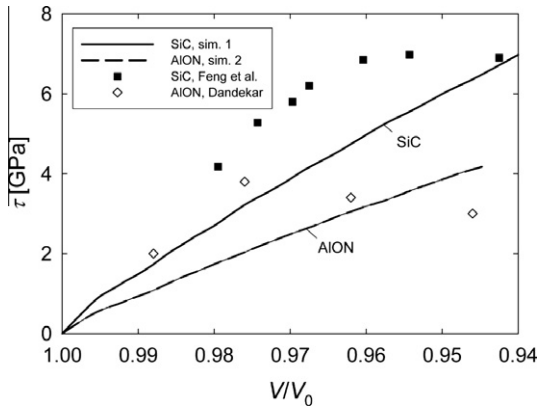
Predicted and experimental shear stress for AlON in uniaxial strain compression.

Simulation or experiment	τ [GPa]				
	$\frac{V}{V_0} = 0.99$	$\frac{V}{V_0} = 0.98$	$\frac{V}{V_0} = 0.97$	$\frac{V}{V_0} = 0.96$	$\frac{V}{V_0} = 0.95$
Simulation 1	0.95	1.74	2.52	3.24	–
Simulation 2	0.93	1.73	2.48	3.19	3.85
Simulation 3	1.05	1.82	2.56	3.26	3.84
Simulation 4	0.91	1.70	2.45	3.20	–
Simulation 5	0.89	1.69	2.42	–	–
Simulation 6	0.92	1.77	2.60	3.44	–
Simulation 7	0.98	1.79	2.61	3.35	–
Experiment (Dandekar et al., 2007)	2.0	3.8	–	3.4	3.0

Table 5

Simulations reported in Tables 3 and 4.

Simulation	Load direction	Orientation	Elasticity
1	X	1	Nonlinear
2	X	2	Nonlinear
3	X	1	Linear
4	Y	1	Nonlinear
5	Y	2	Nonlinear
6	Y	1	Linear
7	Z	1	Nonlinear

**Fig. 6.** Shear stress: present simulations (nonlinear elasticity and fracture) and experiments.

order of several percent. Linear elastic models do not always provide an increase in shear stress relative to complementary nonlinear elastic models, in contrast to axial stresses and pressures which are larger when nonlinear theory is used. Shear stresses from representative simulations are compared graphically with experimental data in Fig. 6.

4.2. Unconfined compression

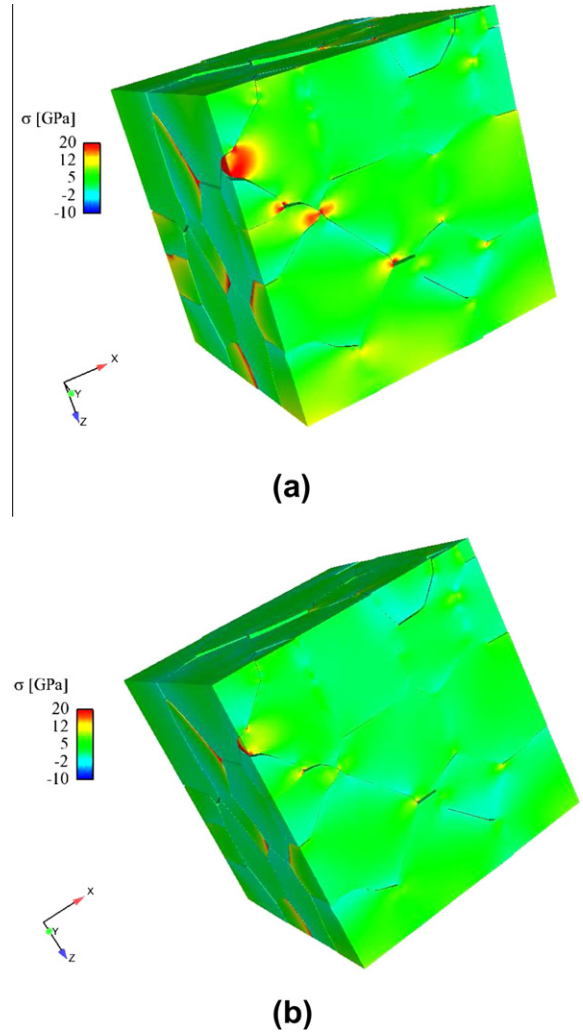
Results for dynamic uniaxial stress loading are reported next. Let X denote the referential direction of loading, with Y and Z denoting orthogonal directions, and with a corner of the cubic specimen located initially at the origin $(X, Y, Z) = (0, 0, 0)$. Boundary conditions and nonzero initial conditions for unconfined compression in the X -direction are, respectively,

$$\begin{aligned} v_x &= -\dot{\epsilon}X \quad \text{along } X = L; \\ v_x &= 0 \quad \text{along } X = 0; \\ \sigma_{ab}n_b &= 0 \quad \text{along } Y, Z = 0, L; \end{aligned} \quad (31)$$

$$v_x(t=0) = -\dot{\epsilon}X \leftrightarrow \partial_x v_x(t=0) = -\dot{\epsilon}. \quad (32)$$

The imposed strain rate is $\dot{\epsilon} = 10^5/\text{s}$. Initial conditions (32) impose a uniform initial velocity gradient throughout the domain. Uniaxial stress simulations were also performed via loading in orthogonal Y and Z directions, with analogous boundary and initial conditions. Under these loading conditions, the average axial strain of the aggregate is $\Delta L/L_0 = \dot{\epsilon}t$, positive in compression. Fully free, as opposed to periodic, boundary conditions are applied to lateral faces of the microstructure.

Fig. 7 shows representative axial stress contours ($\sigma = -\sigma_{xx}$, positive in compression) in SiC (Fig. 7(a)) and AION (Fig. 7(b)). In each case shown, a 50-grain microstructure is deformed to 2% strain, i.e., $\Delta L/L_0 = 0.02$ via compression along the X -direction. Stresses are somewhat higher in SiC than AION as a result of the larger elastic

**Fig. 7.** Axial stress σ (positive in compression) for 50-grain microstructures subjected to unconfined axial strain of $\Delta L/L_0 = 0.02$: (a) SiC (b) AION.

stiffness and higher fracture strength and toughness in the former (Tables 1 and 2). In each microstructure, cracks associated with axial splitting appear, as do sliding cracks associated with dilatation (i.e., expansion) in directions orthogonal to the loading direction. Fractures are more profuse, and stresses are significantly lower, than those observed in uniaxial strain compression (Section 4.1, Fig. 3).

Tables 6 and 7 show peak axial stress and corresponding failure strain data for SiC and AION microstructures. Nonlinear elasticity has been used in obtaining all model results shown. Peak axial stress Σ^f is defined as the maximum value of average compressive stress Σ attained over the duration of an experiment/simulation prior to strain softening associated with damage/fracture, and peak strain ϵ^f is the corresponding average compressive strain, i.e., $\partial \Sigma / \partial (\Delta L/L_0) \approx 0$ at $\Delta L/L_0 = \epsilon^f$. Also shown for purposes of comparison are peak stress data from Kolsky bar experiments at strain rates on the order of $10^3/\text{s}$ (Pickup and Barker, 1997; Wang and Ramesh, 2004; Paliwal et al., 2008). Predicted failure stresses for SiC are smaller than experimental values (Pickup and Barker, 1997; Wang and Ramesh, 2004); furthermore, strain rates considered in the simulations are significantly higher ($10^5/\text{s}$), and brittle materials can exhibit an increase in peak compressive strength with increasing strain rate (Grady, 1998; Chen and Ravichandran, 2000). Predicted strengths for AION are comparable to experimental values

Table 6

Peak axial stress and failure strain for unconfined compression, SiC.

Model/experiment	Load direction	Orientation	ϵ^f [%]	Σ^f [GPa]	Σ^f/t^c
Model	X	1	2.43	4.19	7.35
Model	Y	1	2.79	4.85	8.51
Model	Y	2	2.89	4.82	8.46
Model	Z	2	2.80	4.92	8.63
Experiment (Pickup and Barker, 1997)	–	–	–	6.72–8.17	
Experiment (Wang and Ramesh, 2004)	–	–	–	5.0–7.5	

Table 7

Peak axial stress and failure strain for unconfined compression, AlON.

Model/experiment	Load direction	Orientation	ϵ^f [%]	Σ^f [GPa]	Σ^f/t^c
Model	X	1	3.03	3.24	10.59
Model	X	2	3.00	3.13	10.22
Model	Y	1	2.89	3.59	11.73
Model	Z	1	3.42	3.76	12.28
Experiment (Paliwal et al., 2008)	–	–	–	3.0–4.0	

(Paliwal et al., 2008). Comparing the rightmost columns of Tables 6 and 7, it is clear that predicted unconfined compressive strengths are not directly proportional to prescribed cohesive strength t^c since the ratio Σ^f/t^c is significantly higher in AlON than in SiC for each reported simulation. Variations in predicted peak strength resulting from differences in lattice orientation (i.e., orientations 1 and 2) appear smaller than variations from differences in loading direction (i.e., X, Y, or Z).

4.3. Shear

Lastly, results for dynamic shear loading with and without superimposed compressive stress are reported. Let X denote the referential direction of loading, with Y and Z denoting orthogonal directions, and with a corner of the cubic specimen located initially at the origin $(X, Y, Z) = (0, 0, 0)$. Three kinds of boundary and initial conditions are considered: unconfined shear, confined shear, and shear+compression. Boundary conditions and nonzero initial conditions for unconfined shear in the X direction on the Y plane are, respectively,

$$\begin{aligned} v_x &= \dot{\gamma}Y \quad \text{along } Y = L, \quad v_x = v_y = v_z = 0 \quad \text{along } Y = 0; \\ \sigma_{yy}n_y &= 0 \quad \text{along } Y = L, \quad \sigma_{ab}n_b = 0 \quad \text{along } X, Z = 0, L; \end{aligned} \quad (33)$$

$$v_x(t=0) = \dot{\gamma}Y \leftrightarrow \partial_y v_x(t=0) = \dot{\gamma}. \quad (34)$$

The imposed shear strain rate is $\dot{\gamma} = 10^5/s$; note that this is equal to twice the imposed deformation rate $\frac{1}{2}(\partial_b v_a + \partial_a v_b)$. Initial conditions (34) impose a uniform initial velocity gradient throughout the domain. Numerous shear simulations were also performed via loading in forward and reverse directions on orthogonal Y and Z planes, providing up to twelve unconfined shear simulations (six off-diagonal components of $\partial_b v_a \times$ two directions (positive and negative)) for each set of {microstructure, material, lattice orientation}. Under these loading conditions, the magnitude of average shear strain of the aggregate is $\gamma = \dot{\gamma}t$.

Boundary conditions and nonzero initial conditions for confined shear in the X direction on the Y plane are, respectively,

$$\begin{aligned} v_x &= \dot{\gamma}Y \quad \text{along } Y = L, \quad v_x = v_y = v_z = 0 \quad \text{along } Y = 0; \\ v_y &= 0 \quad \text{along } Y = L, \quad \sigma_{ab}n_b = 0 \quad \text{along } X, Z = 0, L; \end{aligned} \quad (35)$$

$$v_x(t=0) = \dot{\gamma}Y \leftrightarrow \partial_y v_x(t=0) = \dot{\gamma}. \quad (36)$$

Conditions (35) differ from those for unconfined compression (33) in only one respect: in the former, the plane on which shearing velocities are applied is prohibited from moving in a direction normal to the shearing direction. This results in an increase in compressive stress in the confined case, since the fixed upper boundary resists dilatation accompanying shear-induced fracture within the aggregate. Initial conditions are the same in either case. Again, particular loading planes and directions are varied among many simulations.

Boundary conditions and nonzero initial conditions for shear+compression in the X direction on the Y plane are, respectively,

$$\begin{aligned} v_x &= \dot{\gamma}Y \quad \text{along } Y = L, \quad v_x = v_y = v_z = 0 \quad \text{along } Y = 0; \\ v_y &= -\dot{\gamma}Y \quad \text{along } Y = L, \quad \sigma_{ab}n_b = 0 \quad \text{along } X, Z = 0, L; \end{aligned} \quad (37)$$

$$\begin{aligned} v_x(t=0) &= \dot{\gamma}Y \leftrightarrow \partial_y v_x(t=0) = \dot{\gamma}; \\ v_y(t=0) &= -\dot{\gamma}Y \leftrightarrow \partial_y v_y(t=0) = -\dot{\gamma}. \end{aligned} \quad (38)$$

Conditions (37) specify simultaneous shear and compression deformation, both at an imposed rate of $\dot{\gamma} = 10^5/s$. Initial conditions (38) provide for a corresponding uniform initial velocity gradient. Again, loading planes and directions are varied among many simulations. In all three cases listed above (unconfined shear, confined shear, and shear+compression), fully free, as opposed to periodic, boundary conditions are applied to lateral faces of the microstructure.

Shown in Fig. 8 are shear stress contours $\sigma = \sigma_{ab}$, where $\partial_b v_a$ is the corresponding component of the applied velocity gradient. The applied shear strain is $\gamma = 0.03$, and material properties are those of AlON. Results in Fig. 8(a) and (b) correspond to unconfined shear (33) and confined shear (35), respectively, of microstructure II. Notice that local stresses are larger in magnitude in the latter case, since the microstructure is unable to expand in the vertical direction to relieve pressure induced by dilatation. The higher pressure leads to an increase in shear stress for the confined condition. Results shown in Fig. 8(c) and (d) correspond to microstructure I (AlON) subjected to shear+compression loading via (37). Results in Fig. 8(d), wherein approximately half of the grains are removed from the image, show stresses in the interior of the microstructure whose exterior is shown in Fig. 8(c). Shear stress magnitudes are significantly greater for simultaneous shear and compression than for shear loading alone.

In all boundary and initial conditions considered in (33)–(38), the microstructure is free to expand or deform in lateral (as opposed to vertical) directions, as is clear from Fig. 8. Effects of restricting motion of the lateral faces are considered in Fig. 9, which shows average shear stress $\bar{\tau}$ for the same aggregate deformed according to confined shear conditions with and without restricting motion of lateral faces. Precisely, average shear stress $\bar{\tau}$ for the present loading conditions is computed analogously to (29):

$$\bar{\tau} = (1/A) \int_A \hat{t}^t dA, \quad (39)$$

where \hat{t}^t is the component of traction acting in the direction of shear, on sheared surface (plane) with area A. The three curves in Fig. 9 all correspond to the same microstructure, loading plane and direction, and lattice orientation distribution, with nonlinear elastic properties for SiC. Fracture is suppressed (i.e., contact between all grains is rigid) for the stiffest case shown in Fig. 9, which has a slope of 191 GPa, very close to the Voigt-average shear modulus G listed in Table 1. This case corresponds to simple shear of an elastic polycrystalline aggregate. When internal fractures are permitted within the microstructure, but lateral boundaries are moved

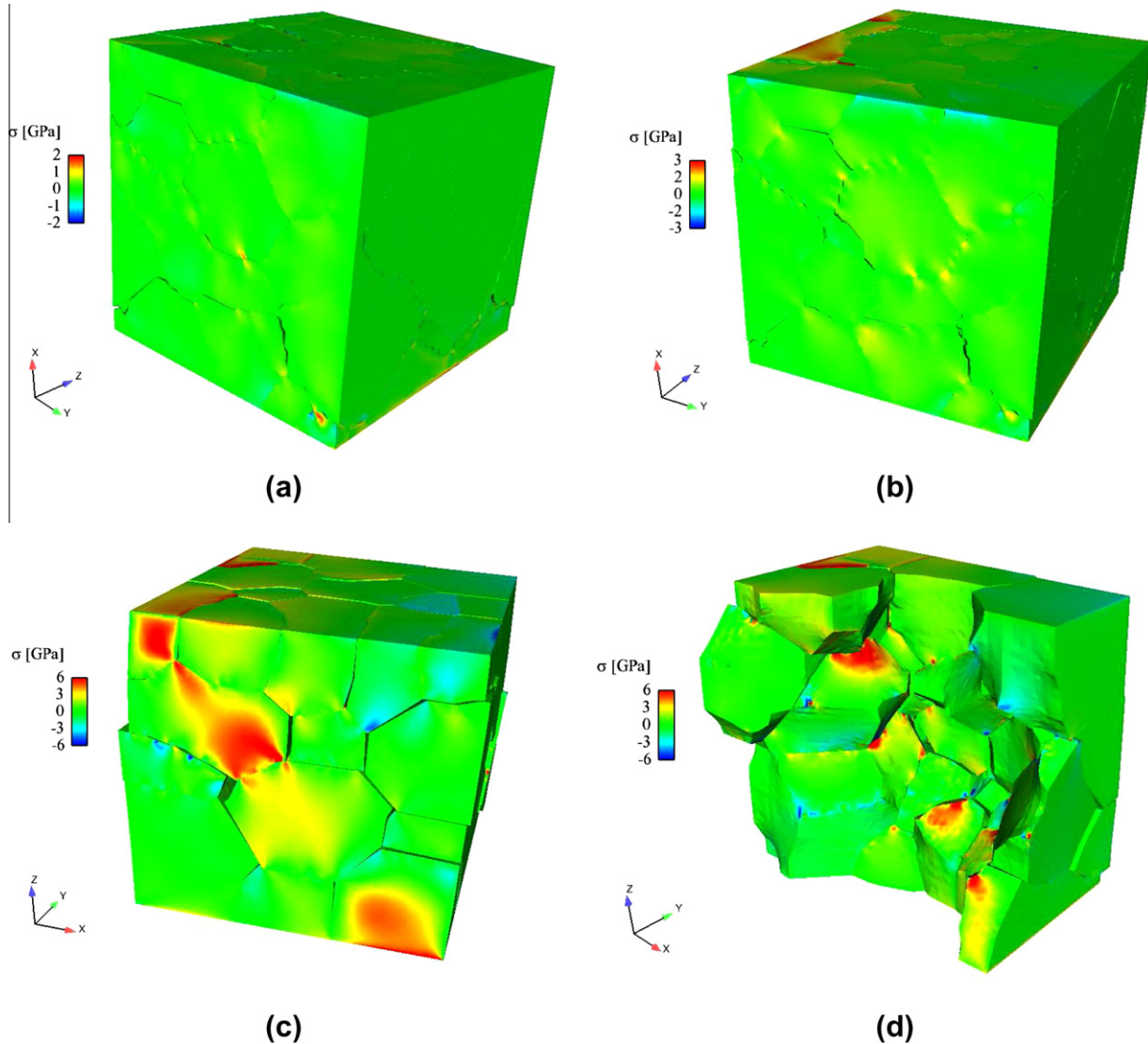


Fig. 8. Shear stress σ for AION microstructures subjected to shear deformation $\gamma = 0.03$: (a) microstructure II, unconfined shear, nonzero $\partial_x v_y$ (b) microstructure II, confined shear, nonzero $\partial_x v_y$ (c) microstructure I, shear+compression, nonzero $\partial_x v_x + \partial_x v_z$ (d) microstructure I, shear+compression, some grains removed for viewing of specimen interior.

rigidly (i.e., in simple shear) and are prohibited from expanding to accommodate dilatation, the intermediate curve in Fig. 9 results. Note that the average shear stress for this case is lower than that for the case with no fracture at applied shear strain $\gamma \gtrsim 0.5\%$, since fracture and crack opening/sliding within the aggregate tends to reduce the overall stiffness of the aggregate. The lowest average shear stresses are exhibited by the unconfined case (i.e., free lateral faces).

Behavior of a polycrystalline aggregate embedded within a much larger sample of material would be expected to exhibit average shear stress behavior falling in between the two lower curves in Fig. 9, which represent Dirichlet and Neumann boundary conditions, respectively, on lateral faces. Periodic boundary conditions (Espinosa and Zavattieri, 2003a,b) would be expected to produce strength falling between these two curves, leading to a more realistic depiction of shearing behavior of a representative volume element of material embedded within a larger sample. However, uniaxial strain conditions for lateral confinement considered in Section 4.1 are deemed representative of plate impact experiments, as has been assumed in previous studies (Clayton, 2005b; Foulk and Vogler, 2010). And free boundary conditions considered

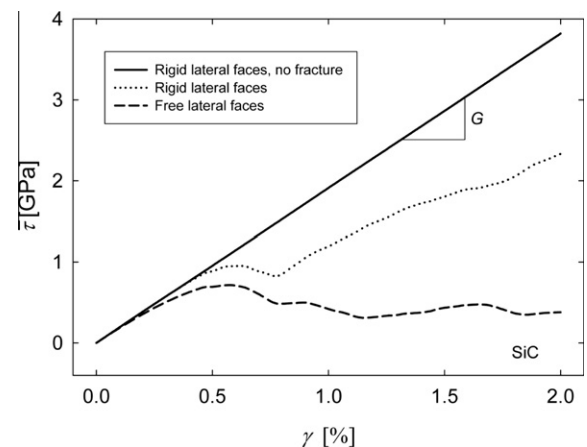


Fig. 9. Average shear stress versus applied shear strain for SiC microstructure I subjected to various lateral boundary conditions.

for unconfined compression in Section 4.2 are deemed more appropriate than periodic boundary conditions for modeling miniature dynamic compression experiments (Paliwal et al., 2008) wherein the actual size of the experimental sample is comparable to that of the simulated polycrystalline aggregate.

Weibull distributions are often used to characterize failure behavior of brittle solids, including polycrystalline ceramics (Warner et al., 2005; Brannon et al., 2007; Foulk and Vogler, 2010; Graham-Brady, 2010; Leavy et al., 2010). Let $\tau \geq 0$ denote an independent variable. A two-parameter Weibull distribution (Hayter, 1996) has a probability density function

$$\hat{f}(\tau) = m\sigma_0^{-m}\tau^{m-1}\exp[-(\tau/\sigma_0)^m], \quad (40)$$

and cumulative distribution function

$$f(\tau) = \int_0^\tau \hat{f}(x)dx = 1 - \exp[-(\tau/\sigma_0)^m], \quad (41)$$

where m is the Weibull modulus and σ_0 is a parameter with the same physical dimensions as τ . Analyzed in what follows next are statistics of failure for numerous simulations involving unconfined shear boundary conditions (33). The shear stress at failure (i.e., the shear strength) τ for a given simulation is defined as the peak stress at which $\partial\bar{\tau}/\partial\gamma = 0$. For simulation results analyzed here, the probability f of failure at or below a given shear stress τ is found by ordering the results of many simulations from lowest to highest shear strength and assigning the j th result in a series of n simulations a failure probability $f_j = \frac{1}{n}(j - \frac{1}{2})$ (Warner et al., 2005; Furnish et al., 2007). A plot of $\ln\{\ln[1/(1-f)]\}$ versus $\ln\tau$ exhibits slope m (the Weibull modulus). A “nominal strength” (Warner et al., 2005) for a series of simulations is calculated as $\sigma_0 = \exp(-b/m)$, where b is the vertical intercept of the linear fit to this plot, noting that $f(\sigma_0) = 1 - \exp(-1) \approx 0.632$. Recall that the higher the value of Weibull modulus m , the lower the variability or scatter in variable τ .

Weibull fits to unconfined strength data collected from many simulations of unconfined dynamic shear are shown in Fig. 10(a) for SiC and Fig. 10(b) for AION. Data from several dozen simulations are considered in each case, incorporating various microstructures, random lattice orientation distributions, and loading directions. Fits to the data are constructed by considering results of each of microstructures I (50 grains) and II (126 grains) individually, as well as data from results of simulations on both microstructures taken together. For each material, microstructure I exhibits a higher Weibull modulus than microstructure II, corresponding to more uniform shear failure statistics. A reduction in

Weibull modulus with increasing sample size has been noted elsewhere from static flexure and indentation experiments on SiC (Wereszczak et al., 2010). However, diametral compression data for SiC (Leavy et al., 2010) demonstrate an increasing Weibull modulus and decreasing median strength with increasing sample size. Comparing Fig. 10(a) and (b), predicted Weibull moduli for AION microstructures are significantly lower than those for SiC.

Table 8 compares Weibull parameters from the present work with those obtained from other modeling (Foulk and Vogler, 2010) and experimental (Klein and Miller, 2001; Warner et al., 2005; Patel et al., 2006; Ray et al., 2007; Furnish et al., 2007; Wereszczak et al., 2010) studies. For the present modeling results, nominal strength σ_0 is substantially greater in SiC (0.52 GPa) than in AION (0.35 GPa), as would be expected from the prescribed interfacial strengths in Table 2: $t_{\text{SiC}}^{\text{c}}/t_{\text{AION}}^{\text{c}} \approx 1.9 > 0.52/0.35 \approx 1.5$. Nominal strength σ_0 does not vary appreciably between results for microstructures I and II, in contrast to Weibull modulus m . Weibull moduli computed for SiC in the present work are significantly larger than those observed in experiments (Ray et al., 2007; Furnish et al., 2007; Wereszczak et al., 2010). Note however that loading conditions considered elsewhere (shock loading, static bending, or static indentation) differ from those considered in the present simulations (dynamic unconfined shear). Furthermore, sample sizes considered in the present work are significantly smaller in terms of number of grains than specimens tested experimentally. Weibull moduli computed in the present work for AION are closer to, but still generally larger than, those measured experimentally (Klein and Miller, 2001; Warner et al., 2005; Patel et al., 2006). It is emphasized that experimental data for Weibull parameters for both materials (SiC and AION) vary significantly from study to study as a result of differences in material samples (e.g., different processing routes leading to variable defect content), experimental loading techniques, and specimen sizes. However, a general trend of lower nominal strength and lower Weibull modulus in AION than in SiC is evident in the experimental values listed in Table 8; furthermore, this trend is qualitatively reflected by the present model predictions.

Table 9 shows peak shear strengths for various simulations involving different materials, microstructures, loading directions, and initial lattice orientation distributions. Unconfined boundary conditions correspond to (33); confined boundary conditions correspond to (35). Directions refer to shearing in positive (+) and negative (−) directions on the same plane of loading. The rightmost column of Table 9 lists the percentage difference in peak strength

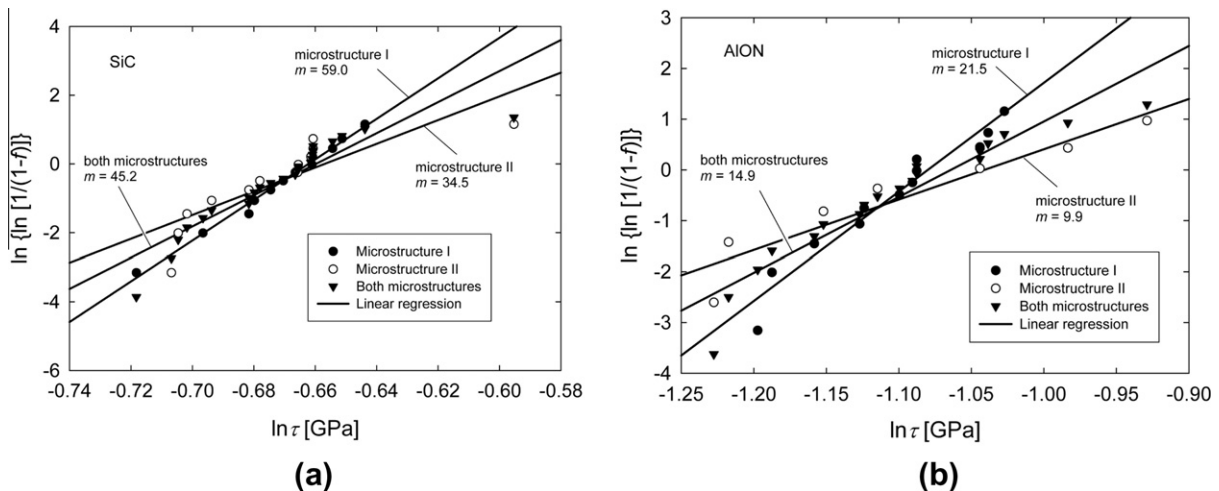


Fig. 10. Weibull fits to all relevant simulation results (multiple microstructures, grain orientations, and loading directions) for peak average unconfined shear strength: (a) SiC (b) AION.

Table 8

Weibull parameters for SiC and AlON.

Model/experiment	Material	Microstructure	Strength	σ_0 [GPa]	m
Model (present)	SiC	I and II	Unconfined shear	0.517	45.2
Model (present)	SiC	I	Unconfined shear	0.516	59.0
Model (present)	SiC	II	Unconfined shear	0.518	34.5
Model (Fouk and Vogler, 2010)	SiC	–	Spall	11.6–12.3	12–18
Experiment (Ray et al., 2007)	SiC	–	Flexure	0.367–0.617	4.9–26.6
Experiment (Furnish et al., 2007)	SiC	–	HEL	10.23–10.33	14.4–29.7
Experiment (Wereszczak et al., 2010)	SiC	–	Indentation	0.876–2.652	13.9–20.1
Experiment (Wereszczak et al., 2010)	SiC	–	Flexure	0.268–0.776	6.6–12.2
Model (present)	AlON	I and II	Unconfined shear	0.345	14.9
Model (present)	AlON	I	Unconfined shear	0.340	21.5
Model (present)	AlON	II	Unconfined shear	0.353	9.9
Experiment (Klein and Miller, 2001)	AlON	–	Flexure	0.315	4.45
Experiment (Warner et al., 2005)	AlON	–	Flexure	0.288–0.812	2.9–26.3
Experiment (Patel et al., 2006)	AlON	–	Indentation	0.228	8.7

for the two lattice orientation sets considered on a given row, quantifying effects of elastic anisotropy. Specifically, this difference is computed as $2(\tau_1 - \tau_2)/(\tau_1 + \tau_2) \times 100\%$, where subscripts refer to orientation sets 1 and 2. Comparing results for SiC and AlON, it appears that anisotropy has a greater effect on shear strength in AlON than in SiC, especially for unconfined boundary conditions. Recall from Table 2 that the Zener anisotropy factor deviates more from unity for AlON (2.38) than SiC (0.83). However, SiC is hexagonal, and additional anisotropy results from $C_{13} \neq C_{12}$ and $C_{33} \neq C_{11}$. Increased variability due to anisotropy would contribute to a lower predicted Weibull modulus in AlON compared to that of SiC. Differences in peak strength due to differences in loading direction (+ versus -) are also generally larger in AlON than in SiC. Because of its lower prescribed cohesive strength and fracture energy, AlON may be more sensitive than SiC to local variations in microstructure geometry (e.g., grain boundary facets oriented favorably for fracture or stress concentrations at triple points) that would lead to fracture initiation and subsequent failure. Variability due to loading direction (i.e., grain morphology) tends to exceed that due to elastic anisotropy. When the material is loaded in forward and reverse directions, different fracture sites can activate. In all simulations, confinement leads to an increase in shear strength relative to the corresponding unconfined case. Normal stress Σ on the confined surface does contribute to computed average shear strength:

$$\tau = \sqrt{J_2} = [(3\bar{\tau}^2 + \Sigma^2)/3]^{1/2}, \quad (42)$$

where J_2 is the second invariant of the average deviatoric shear stress. For unconfined shear, $\Sigma = 0$ and $\tau = \bar{\tau}$.

4.4. Summary and discussion

Considered collectively, results presented in Sections 4.1, 4.2 and 4.3 demonstrate increasing shear strength with increasing average pressure for both SiC and AlON polycrystals. Relationships between shear strength $\tau = \sqrt{J_2}$ and average pressure P are shown in Fig. 11(a) for SiC and (b) for AlON. Strength corresponds to the peak value of average shear stress defined in (42) for unconfined compression (i.e., $\tau = \Sigma/\sqrt{3}$ for uniaxial stress compression), or for shear loading with or without confinement or superimposed compression. For uniaxial strain loading, following previous models (Lee et al., 2005; Brannon et al., 2007; Leavy et al., 2010), the shear strength from (30), multiplied by $2/\sqrt{3}$ to be consistent with $\sqrt{J_2}$, taken at the compressive strain (i.e., current volume) corresponding to the Hugoniot elastic limit (HEL) is used: $V/V_0 = 0.975$ for SiC (Clayton, 2010c; Feng et al., 1998) and $V/V_0 = 0.970$ for AlON (Clayton, 2011a; Dandekar et al., 2007). Average pressure is always computed via the second of (30) and vanishes for unconfined shear loading. The horizontal intercept at null shear strength (i.e., the hydrostatic tensile strength) follows directly from the prescribed cohesive strength of each material (Table 1) as $-t^c/3$.

Also shown in Fig. 11 are analytical fits (solid lines) to the present model results (SiC and AlON) and fits to experimental data (Lee et al., 2005) (SiC only). Comprehensive shear strength versus pressure data (experimental or numerical) for AlON have not been published elsewhere, to the authors' knowledge. Two functional forms are shown. The first, which has been used elsewhere for SiC (Lee et al., 2005), follows from a cap plasticity model formulated in the context of geomechanics (Sandler and Rubin, 1979):

Table 9

Representative peak shear strengths for SiC and AlON: various microstructures, loading directions, and lattice orientation distributions.

Material	Micro-	Boundary Condition	Loading Direction	τ [GPa] Orientation 1	τ [GPa] Orientation 2	Difference [%]
SiC	I	Unconfined	+	0.521	0.525	0.8
SiC	I	Unconfined	–	0.514	0.516	0.4
SiC	I	Confined	+	0.715	0.713	0.3
SiC	I	Confined	–	0.696	0.704	1.1
SiC	II	Unconfined	+	0.506	0.500	1.2
SiC	II	Unconfined	–	0.496	0.493	0.6
SiC	II	Confined	+	0.643	0.630	2.0
SiC	II	Confined	–	0.636	0.631	0.8
AlON	I	Unconfined	+	0.314	0.333	5.9
AlON	I	Unconfined	–	0.352	0.302	15.3
AlON	I	Confined	+	0.432	0.416	3.8
AlON	I	Confined	–	0.472	0.475	0.6
AlON	II	Unconfined	+	0.325	0.395	19.4
AlON	II	Confined	+	0.402	0.407	1.2

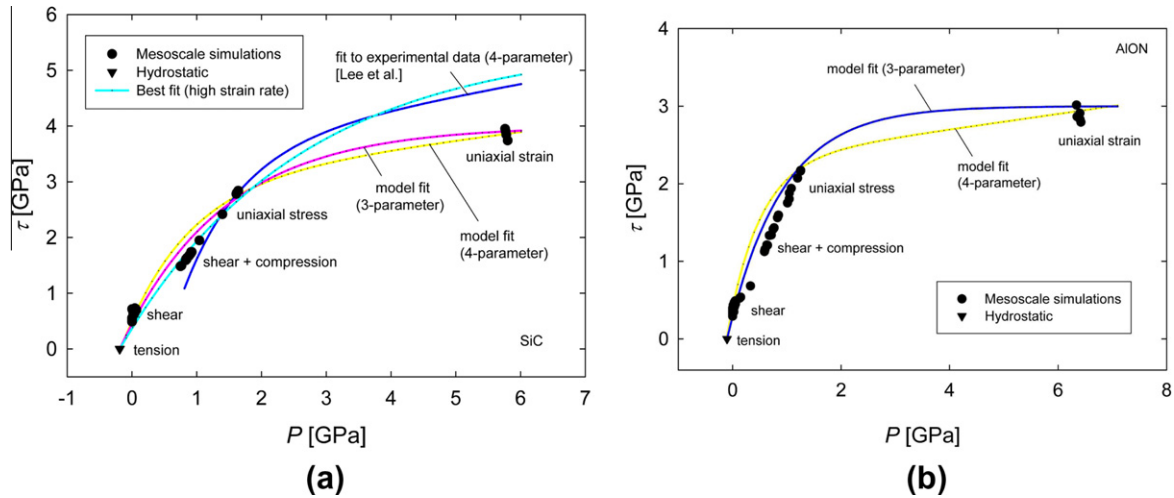


Fig. 11. Average shear strength versus average pressure for all relevant simulation results (multiple microstructures, grain orientation distributions, loading directions, and confinement conditions): (a) SiC (b) AlON.

$$\tau = a_1 - a_2 \exp(-a_3 P) + a_4 P, \quad (43)$$

where a_1, a_2, a_3 , and a_4 are constants. Notice that the constants are labeled slightly differently here than in Lee et al. (2005); all constants in (43) are positive in sign and P is positive in compression. The second follows from a continuum damage mechanics model used for ceramics under impact loading (Leavy et al., 2010):

$$\tau = b_1 \{1 - \exp[-(b_2/b_1)(b_3 + P)]\}, \quad (44)$$

where b_1, b_2 , and b_3 are constants. Parameters for each fit are listed in Table 10.

First consider numerical data from the present simulations. In each material, the increase in shear strength with compressive pressure or confinement is evident. Previous models (Brannon et al., 2007, 2009; Leavy et al., 2010) have assumed that variability in strength decreases with an increase in pressure. This phenomenon is not apparent from the present results. Percentage-wise, differences in strength from simulation to simulation are of the same order of magnitude for unconfined and confined loading, as is evident from Tables 3, 4, and 9. Overall, the shear stiffness of SiC is greater than that of AlON because of the greater prescribed elastic stiffness (e.g., second-order elastic constants), fracture strength, and fracture energy in the former. The analytical fit to experimental results for SiC (Lee et al., 2005) exhibits higher strength than the present model results at high pressures and lower strength than the present results at low pressures; however, the fit to experimental results is valid only for the pressure regime shown and does not extrapolate correctly to lower compressive pressures or the tensile regime. Also shown in Fig. 11(a) is a “best fit” to combined experimental and numerical data deemed most appropriate for dynamic behavior of SiC over the entire pressure regime shown.

Table 10
Parameters for pressure-dependent strength models of SiC and AlON.

Parameter	SiC (simulation)	SiC (Lee et al., 2005)	SiC (best fit)	AlON (simulation)
a_1 [GPa]	3.0	3.5	–	2.3
a_2 [GPa]	2.5	6.3	–	1.9
a_3 [1/GPa]	1.0	1.1	–	1.7
a_4	0.15	0.21	–	0.1
b_1 [GPa]	4.0	–	5.5	3.0
b_2	2.5	–	2.0	3.0
b_3 [GPa]	0.19	–	0.19	0.10

Table 11 summarizes pressure-strength behavior for SiC obtained from various models and experiments. At higher pressures, mesoscale simulation data fit to (44) provides a lower strength than other models and plate impact experiments. The “best fit” to (44) matches strength data reported by (Lee et al., 2005, p. 25) at $P = 10$ GPa but gives a lower shear strength than that reported in Feng et al. (1998). The “JH-1” model (Holmquist and Johnson, 2002) provides stiffer shear strength versus pressure behavior than the present model fits when the ceramic is considered intact, but much lower strength when the ceramic has “failed” due to plastic strain accumulation.

Parameters listed in Tables 8 and 10 can be used directly in macroscopic models of inelasticity and failure of ceramic materials incorporating Weibull statistics and pressure-dependent shear strength (Brannon et al., 2007, 2009; Leavy et al., 2010). The present results may be particularly valuable for AlON, for which experimental data (statistical and pressure-strength) are not as readily available. The present modeling effort considers sample sizes (1 mm^3 , ~ 100 grains) commensurate with finite element sizes used in macroscopic applications (Brannon et al., 2007; Leavy et al., 2010). Furthermore, strain rates considered are applied uniformly to the microstructure through appropriate boundary conditions and initial conditions on the velocity gradient, and are of

Table 11
Strength ($\tau = \sqrt{J_2}$) versus pressure (P or mean stress) for SiC.

Model or experiment	Loading	P [GPa]	τ [GPa]
Mesoscale simulation (Eq. (44))	Uniaxial strain $10^5/\text{s}$	1.0	2.1
		5.0	3.8
		10.0	4.0
Best fit (Eq. (44))	Various	1.0	2.0
		5.0	4.7
		10.0	5.4
JH-1 intact (Holmquist and Johnson, 2002)	Uniaxial strain $10^5/\text{s}$	1.0	2.4
		5.0	5.6
		10.0	7.8
JH-1 failed (Holmquist and Johnson, 2002)	Uniaxial strain $10^5/\text{s}$	≥ 3.3	0.8
Experiment (Feng et al., 1998)	Plate impact	4.6	4.8
		5.5	5.2
		9.7	7.9
Experiment (Lee et al., 2005)	Plate impact	10.0	5.4

magnitude pertinent to ballistic events ($10^5/s$). This is in contrast to static data (Lee et al., 2005), extrapolated to the dynamic regime, often used to parameterize such models at lower confining pressures in the absence of very high-rate data (Brannon et al., 2007, 2009; Leavy et al., 2010). Simulation results may also be used to inform macroscopic models explicitly considering crack opening displacements in the context of large deformation kinematics (Clayton and McDowell, 2003, 2004; Clayton, 2005a, 2010a); such an effort may be pursued in future work. The present results suggest two features of current macroscopic ceramic models that warrant further consideration and possible refinement: (i) possible size dependence of the Weibull modulus and (ii) statistical variability in shear strength at various pressures and loading rates. Existing models (Brannon et al., 2007, 2009; Leavy et al., 2010) consider a constant Weibull modulus for hydrostatic tensile strength and assume reduced variability in strength at high pressures (e.g., in the regime of plate impact or uniaxial strain experiments).

Predictions of the present work follow from a number of modeling assumptions. Possible limitations of the present modeling effort are enumerated below:

1. Grain structures considered are synthetic, with random initial lattice orientation distributions used to specify anisotropic elastic constants. Greater physical realism would be attained from finite element meshes of microstructures obtained from sectioned material samples, with initial lattice orientation distributions obtained from EBSD measurements, for example (Brahme et al., 2006; Rollett et al., 2007). In particular, SiC-N can often exhibit relatively elongated grains (Lee et al., 2005; Ray et al., 2007; Vargas-Gonzalez et al., 2010), whereas AlON often exhibits relatively equiaxed grains (Corbin, 1989; McCauley et al., 2009; Guo et al., 2011).
2. Dislocation-mediated plasticity and twinning are not considered. When confining pressures and shear stresses are large, fracture may be suppressed and dislocation motion may occur in ceramics. In hexagonal polytypes of SiC, partial dislocation motion on basal planes and associated stacking fault propagation are thought to be the prominent mode of plastic deformation (Zhang et al., 2005b,a; Clayton, 2010c). In AlON, dislocation slip and twinning on octahedral planes has been observed in experiments (Paliwal et al., 2008; McCauley et al., 2009) and modeled with crystal plasticity theory (Gazonas et al., 2010; Clayton, 2011a).
3. Significant uncertainty exists for some elastic properties. Complete second-order elastic constants have been measured for SiC (Kamitani et al., 1997). The remaining elastic properties listed in Table 1 are theoretical predictions. Pressure dependencies of second-order elastic coefficients of SiC follow from atomic modeling (Davydov, 2004). Anisotropic second-order elastic constants for AlON have been computed using first principles (Gazonas et al., 2010), as have pressure dependencies of second-order elastic coefficients (Batyrev et al., 2011). Recent indentation experiments suggest that AlON may be highly elastically anisotropic (Guo et al., 2011), in qualitative agreement with anisotropic constants used in the present work but contradicting previous work wherein nearly isotropic elastic constants were used (Clayton, 2011a).
4. Uniform cohesive properties (i.e., fracture strength and fracture energy) are assigned to all grain boundaries in a given microstructure. In real ceramic polycrystals, variability in fracture properties may arise from voids, inclusions, and secondary phases, though in some cases secondary phases may be incorporated deliberately to improve fracture toughness (Faber and Evans, 1983; Shih et al., 1998; Vargas-Gonzalez et al., 2010). Grain boundary misorientation may also influence local fracture properties. Highly non-uniform grain boundary properties would be expected to result in greater variability in predicted failure statistics, e.g., lower Weibull moduli. In principle, grain boundary strengths could be seeded to enable simulation results to match experimental failure statistics. However, for statistics obtained from numerical simulations to be labeled as truly predictive, input parameters for mesoscale models should be obtained from independent experiments that measure local property distributions, or from atomic theory (Kohyama, 1999), rather than calibrated to match macroscopic failure data.
5. Contact is assumed frictionless between grain boundary facets. Some sliding friction might be expected between failed surfaces, as has been considered in previous models (Kraft and Molinari, 2008; Kraft et al., 2008). Incorporation of frictional sliding would presumably increase predicted shear strengths of polycrystalline aggregates, especially at higher confining pressures. In particular, omission of contact friction may, at least partially, explain the lower compressive and shear stresses predicted for SiC microstructures in the present simulations relative to corresponding experimental data.
6. Porosity is not considered. Polycrystalline ceramics are not fully dense, with measured porosities in SiC and AlON on the order of one to several percent (Graham et al., 1988; Lee et al., 2005; Dandekar et al., 2007). Pore collapse can influence the high pressure response of ceramics and geologic solids, e.g., resulting in increased compressibility relative to a fully dense material (Clayton, 2008, 2011a).
7. Transgranular failures, i.e., cleavage fractures, are not addressed. Failure in SiC-N is predominantly intergranular (Faber and Evans, 1983; Shih et al., 1998; Lee et al., 2005), although transgranular fractures are observed to a lesser extent (Ray et al., 2007). Transgranular fracture has been observed in AlON deformed at high rates (Paliwal et al., 2008; McCauley et al., 2009) and in static indentation experiments (Guo et al., 2011).
8. Adiabatic conditions are assumed, with isentropic elastic behavior used for single crystals within each microstructure. In real materials, plastic deformation, twinning, pore collapse, and frictional sliding at fractured interfaces could all contribute to dissipation (i.e., entropy production) and temperature rise at high rates of loading. If such effects are significant, consideration of thermal expansion, temperature dependent elastic coefficients, and temperature dependent cohesive properties (Clayton, 2005b) may be warranted.
9. Boundary and initial conditions used in simulations may deviate from those encountered in experiments to which some results have been compared. Specifically, the present uniaxial strain simulations assign homogeneous compression, omitting the shock process that occurs in plate impact tests. The present shear and shear+compression simulations assign free conditions on lateral faces; periodic boundary conditions might be expected to offer a more realistic representation of bulk material behavior and provide somewhat greater strength and stiffness.

In the context of the above limitations, the present results provide a basis for comparison with future work in which more physical details can be incorporated, e.g., reconstructed actual microstructures, dislocations, twins, initial defect distributions, and transgranular fracture.

5. Conclusions

Numerous three-dimensional finite element simulations of dynamic deformation and fracture of polycrystalline ceramic microstructures have been conducted. Uniaxial strain compression, unconfined compression, and shear loading (with and without

confinement) have been considered. Single crystal deformations have been modeled using nonlinear anisotropic hyperelasticity. Intergranular fractures have been modeled using cohesive zone theory with fracture strength and fracture energy obtained from macroscopic flexure data. Properties are representative of SiC and AlON. Various microstructures, lattice orientation distributions, and loading directions have been considered. Failure statistics have been analyzed.

Results obtained provide new insight into dynamic behavior of ceramic polycrystals for small specimen sizes and loading conditions (e.g., uniform velocity gradient boundary and initial conditions at very high strain rates) not accessible through traditional experiments such as plate impact-driven shock compression or Kolsky bar compression. Key findings are summarized as follows:

- Shear strength of polycrystalline aggregates increases with confining pressure in both materials, in qualitative agreement with experimentally observed trends for brittle solids. Confinement inhibits dilatation associated with interfacial sliding among misaligned grains, leading to an increase in shear stress necessary for mode II crack propagation. Analytical fits to pressure-strength data have been developed for use in macroscopic models of inelasticity in SiC and AlON ceramics.
- For uniaxial strain compression, predicted average axial stresses agree favorably with experimental plate impact data on larger specimens of AlON, but are lower than experimental values for SiC by up to 10–20%. Predicted average shear stresses in both materials are in close agreement with experimental values at higher pressures (e.g., at 5% volumetric compression), but are lower than experimental values at lower pressures.
- In both materials, the predicted Weibull modulus for average unconfined shear strength tends to decrease with an increase in number of grains contained in the microstructure, in qualitative agreement with some experimental observations of decreasing Weibull modulus with increasing sample size.
- Predicted Weibull parameters for shear strength are smaller for AlON than SiC, reflecting lower mean strength and greater variability in the former, in qualitative agreement with experiments. It is suspected that the lower prescribed cohesive strength and toughness for AlON contribute to an increased sensitivity to fracture initiation at interfaces or triple junctions most favorably oriented for fracture.
- Shear failure behavior of AlON appears more sensitive to initial lattice orientation than corresponding behavior of SiC microstructures with the same grain morphology, suggesting a greater sensitivity to elastic anisotropy in the former.

The above conclusions follow from analysis of numerical simulations incorporating idealized microstructures and idealized fracture behavior, without consideration of defects such as pre-existing flaws, voids, inclusions, dislocations, or deformation twins. Thus, the present work should be viewed as a reference against which future studies incorporating such defects can be compared.

Acknowledgements

Prof. A.D. Rollett's research group (Carnegie Mellon University), supported in part by the PETTT program, is thanked for supplying several surface meshes (STL files) of polycrystalline microstructures used in this study.

References

Batyrev, I., McCauley, J., Rice, B., Gazonas, G., Oganov, A., 2011. Atomic structure and elastic properties at high pressure of aluminum oxynitride in cubic phase. In: APS March Meeting. Bulletin of the American Physical Society, Dallas TX.

- Brahme, A., Alvi, M., Saylor, D., Fridy, J., Rollett, A., 2006. 3D reconstruction of microstructure in a commercial purity aluminum. *Scripta Mater.* 55, 75–80.
- Brannon, R., Wells, J., Strack, O., 2007. Validating theories for brittle damage. *Met. Mater. Trans. A* 38, 2861–2868.
- Brannon, R., Fossum, A., Strack, O., 2009. Kayenta: theory and user's guide, Technical Report SAND2009-2282, Sandia National Laboratories, Albuquerque NM.
- Cazamias, J., Fiske, P., Bless, S., 2001. Shock properties of AlON. In: Staudhammer, K., Murr, L., Meyers, M. (Eds.), *Fundamental Issues and Applications of Shock-Wave and High-Strain-Rate Phenomena*. Elsevier, New York, pp. 181–188.
- Chen, W., Ravichandran, G., 2000. Failure mode transition in ceramics under dynamic multiaxial compression. *Int. J. Fracture* 101, 141–159.
- Clayton, J., 2005a. Dynamic plasticity and fracture in high density polycrystals: constitutive modeling and numerical simulation. *J. Mech. Phys. Solids* 53, 261–301.
- Clayton, J., 2005b. Modeling dynamic plasticity and spall fracture in high density polycrystalline alloys. *Int. J. Solids Struct.* 42, 4613–4640.
- Clayton, J., 2006a. Continuum multiscale modeling of finite deformation plasticity and anisotropic damage in polycrystals. *Theor. Appl. Fract. Mech.* 45, 163–185.
- Clayton, J., 2006b. Plasticity and spall in high density polycrystals: modeling and simulation. In: Furnish, M., Elert, M., Russell, T., White, C. (Eds.), *Shock Compression of Condensed Matter Conference Proceedings*. AIP, pp. 311–314.
- Clayton, J., 2008. A model for deformation and fragmentation in crushable brittle solids. *Int. J. Impact Eng.* 35, 269–289.
- Clayton, J., 2009a. A continuum description of nonlinear elasticity, slip, and twinning, with application to sapphire. *Proc. R. Soc. Lond. A* 465, 307–334.
- Clayton, J., 2009b. Modeling effects of crystalline microstructure, energy storage mechanisms, and residual volume changes on penetration resistance of precipitate-hardened aluminum alloys. *Compos. B Eng.* 40, 443–450.
- Clayton, J., 2010a. Deformation, fracture, and fragmentation in brittle geologic solids. *Int. J. Fracture* 163, 151–172.
- Clayton, J., 2010b. Modeling finite deformations in trigonal ceramic crystals with lattice defects. *Int. J. Plasticity* 26, 1357–1386.
- Clayton, J., 2010c. Modeling nonlinear electromechanical behavior of shocked silicon carbide. *J. Appl. Phys.* 107, 013520.
- Clayton, J., 2011a. A nonlinear thermomechanical model of spinel ceramics applied to aluminum oxynitride (AlON). *J. Appl. Mech.* 78, 011013.
- Clayton, J., 2011b. *Nonlinear Mechanics of Crystals*. Springer, Dordrecht.
- Clayton, J., McDowell, D., 2003. Finite polycrystalline elastoplasticity and damage: multiscale kinematics. *Int. J. Solids Struct.* 40, 5669–5688.
- Clayton, J., McDowell, D., 2004. Homogenized finite elastoplasticity and damage: theory and computations. *Mech. Mater.* 36, 799–824.
- Corbin, N., 1989. Aluminum oxynitride spinel: a review. *J. Euro. Ceram. Soc.* 5, 143–154.
- Curran, D., Seaman, L., Cooper, T., Shockey, D., 1993. Micromechanical model for comminution and granular flow of brittle material under high strain rate application to penetration of ceramic targets. *Int. J. Impact Eng.* 13, 53–83.
- Dandekar, D., Bartowski, P., 2001. Spall strengths of silicon carbide under shock loading. In: Staudhammer, K., Murr, L., Meyers, M. (Eds.), *Fundamental Issues and Applications of Shock-Wave and High-Strain-Rate Phenomena*. Elsevier, New York, pp. 71–77.
- Dandekar, D., Vaughan, B., Proud, W., 2007. Shear strength of aluminum oxynitride. In: Elert, M., Furnish, M., Chau, R., Holmes, N., Nguyen, J. (Eds.), *Shock Compression of Condensed Matter Conference Proceedings*. AIP, pp. 505–508.
- Davydov, S., 2004. Effect of pressure on the elastic properties of silicon carbide. *Phys. Solid State* 46, 1200–1205.
- Espinosa, H., Zavattieri, P., 2003a. A grain level model for the study of failure initiation and evolution in polycrystalline brittle materials Part I: Theory and numerical implementation. *Mech. Mater.* 35, 333–364.
- Espinosa, H., Zavattieri, P., 2003b. A grain level model for the study of failure initiation and evolution in polycrystalline brittle materials Part II: Numerical examples. *Mech. Mater.* 35, 365–394.
- Faber, K., Evans, A., 1983. Intergranular crack-deflection toughening in silicon carbide. *J. Amer. Ceram. Soc.* 66, C94–C96.
- Feng, R., Raiser, G., Gupta, Y., 1998. Material strength and inelastic deformation of silicon carbide under shock wave compression. *J. Appl. Phys.* 83, 79–86.
- Foulk, J., Vogler, T., 2010. A grain-scale study of spall in brittle materials. *Int. J. Fracture* 163, 225–242.
- Furnish, M., Vogler, T., Alexander, C., Reinhart, W., Trott, W., Chhabildas, L., 2007. Statistics of the Hugoniot elastic limit from line VISAR. In: Elert, M., Furnish, M., Chau, R., Holmes, N., Nguyen, J. (Eds.), *Shock Compression of Condensed Matter Conference Proceedings*. AIP, pp. 521–524.
- Gailly, B., Espinosa, H., 2002. Modelling of failure mode transition in ballistic penetration with a continuum model describing microcracking and flow of pulverized media. *Int. J. Numer. Methods Eng.* 54, 365–398.
- Gazonas, G., McCauley, J., Kraft, R., Love, B., Clayton, J., Casem, D., Rice, B., Batyrev, I., Weingarten, N., Schuster, B., 2010. Multiscale modeling of armor ceramics: focus on AlON. In: *Proceedings 27th Army Science Conference*, Orlando FL.
- Grady, D., 1998. Shock-wave compression of brittle solids. *Mech. Mater.* 29, 181–203.
- Graham-Brady, L., 2010. Statistical characterization of meso-scale uniaxial compressive strength in brittle materials with randomly occurring flaws. *Int. J. Solids Struct.* 47, 2398–2413.
- Graham, E., Munly, W., McCauley, J., Corbin, N., 1988. Elastic properties of polycrystalline aluminum oxynitride spinel and their dependence on pressure, temperature, and composition. *J. Amer. Ceram. Soc.* 71, 807–812.
- Guo, J., Wang, K., Fujita, T., McCauley, J., Singh, J., Chen, M., 2011. Nanoindentation characterization of deformation and failure of aluminum oxynitride. *Acta Mater.*, 1671–1679.

- Hankey, R., Schuele, D., 1970. Third-order elastic constants of Al_2O_3 . *J. Acoust. Soc. Amer.* 48, 190–202.
- Hayter, A., 1996. *Probability and Statistics for Engineers and Scientists*. PWS Publishing Co., Boston.
- Heard, H., Cline, C., 1980. Mechanical behaviour of polycrystalline BeO , Al_2O_3 and AlN at high pressure. *J. Mater. Sci.* 15, 1889–1897.
- Holmquist, T., Johnson, G., 2002. Response of silicon carbide to high velocity impact. *J. Appl. Phys.* 91, 5858–5866.
- Jung, J., 2010. Presto 4.16 user's guide. Tech. Rep. SAND2010-3112, Sandia National Laboratories, Albuquerque NM.
- Kamitani, K., Grimsditch, M., Nipko, J., Loong, C., Okada, M., Kimura, I., 1997. The elastic constants of silicon carbide: a Brillouin-scattering study of 4H and 6H SiC single crystals. *J. Appl. Phys.* 82, 3152–3154.
- Klein, C., Miller, R., 2001. How to do a Weibull statistical analysis of flexural strength data: application to AlON, diamond, zinc selenide, and zinc sulfide. In: *Proceedings of SPIE*, vol. 4375, Orlando FL, pp. 241–257.
- Kohyama, M., 1999. Tensile strength and fracture of a tilt grain boundary in cubic SiC: a first-principles study. *Phil. Mag. Lett.* 79, 659–672.
- Kraft, R., Molinari, J., 2008. A statistical investigation of the effects of grain boundary properties on transgranular fracture. *Acta Mater.* 56, 4739–4749.
- Kraft, R., Molinari, J., Ramesh, K., Warner, D., 2008. Computational micromechanics of dynamic compressive loading of a brittle polycrystalline material using a distribution of grain boundary properties. *J. Mech. Phys. Solids* 56, 2618–2641.
- Kraft, R., Batyrev, I., Lee, S., Rollett, A., Rice, B., 2010. Multiscale modeling of armor ceramics. In: Swab, J. (Ed.), *Ceramic Engineering Science*. Proceedings of Advanced Ceramic Armor VI. Wiley, Hoboken NJ, pp. 143–158.
- LaSalvia, J., Campbell, J., Swab, J., McCauley, J., 2010. Beyond hardness: ceramics and ceramic-based composites for protection. *JOM* 62, 16–23.
- Leavy, R., Brannon, R., Strack, O., 2010. The use of sphere indentation experiments to characterize ceramic damage models. *Int. J. Appl. Ceram. Tech.* 7, 606–615.
- Lee, M., Brannon, R., Bronowski, D., 2005. Uniaxial and triaxial compression tests of silicon carbide ceramics under quasi-static loading condition. Tech. Rep. SAND2004-6005, Sandia National Laboratories, Albuquerque NM.
- McCauley, J., Patel, P., Chen, M., Gilde, G., Strassburger, E., Paliwal, B., Ramesh, K., Dandekar, D., 2009. AlON: a brief history of its emergence and evolution. *J. Euro. Ceram. Soc.* 29, 223–236.
- Paliwal, B., Ramesh, K., McCauley, J., Chen, M., 2008. Dynamic compressive failure of AlON under controlled planar confinement. *J. Amer. Ceram. Soc.* 91, 3619–3629.
- Patel, P., Swab, J., Staley, M., Quinn, G., 2006. Indentation size effect (ISE) of transparent AlON and MgAl_2O_4 . Tech. Rep. ARL-TR-3852, US Army Research Laboratory, Aberdeen Proving Ground MD.
- Pickup, I., Barker, A., 1997. Damage kinetics in silicon carbide. In: Schmidt, S., Dandekar, D., Forbes, J. (Eds.), *Shock Compression of Condensed Matter Conference Proceedings*. AIP, pp. 513–516.
- Ray, D., Flinders, R., Anderson, A., Cutler, R., Campbell, J., Adams, J., 2007. Effect of microstructure and mechanical properties on the ballistic performance of SiC-based ceramics. In: Franks, L. (Ed.), *Ceramic Engineering Science*. Proceedings of Advanced Ceramic Armor II. Wiley, Hoboken NJ, pp. 85–96.
- Rice, R., Wu, C., Boichelt, F., 1994. Hardness-grain-size relations in ceramics. *J. Amer. Ceram. Soc.* 77, 2539–2553.
- Rollett, A., Manohar, P., 2004. The Monte Carlo method. In: Raabe, D., Roters, F., Barlat, F., Chen, L.-Q. (Eds.), *Continuum Scale Simulation of Engineering Materials*. Wiley-VCH, Weinheim Germany, pp. 77–114.
- Rollett, A., Lee, S., Campman, R., Rohrer, G., 2007. Three-dimensional characterization of microstructure by electron back-scatter diffraction. *Ann. Rev. Mater. Res.* 37, 627–658.
- Sandler, I., Rubin, D., 1979. An algorithm and a modular subroutine for the cap model. *Int. J. Numer. Anal. Methods Geomech.* 3, 173–186.
- Shih, C., Nesterenko, V., Meyers, M., 1998. High-strain-rate deformation and comminution of silicon carbide. *J. Appl. Phys.* 83, 4660–4671.
- Shockey, D., Marchand, A., Skaggs, S., Cort, G., Burkett, M., Parker, R., 1990. Failure phenomenology of confined ceramic targets and impacting rods. *Int. J. Impact Eng.* 9, 263–275.
- Sternberg, J., 1989. Material properties determining the resistance of ceramics to high velocity penetration. *J. Appl. Phys.* 65, 3417–3424.
- Thurston, R., 1974. *Waves in Solids*. In: Truesdell, C. (Ed.), *Handbuch der Physik VIA/4*. Springer-Verlag, Berlin, pp. 109–308.
- Thurston, R., McSkimin, H., Andreatch, P., 1966. Third-order elastic coefficients of quartz. *J. Appl. Phys.* 37, 267–275.
- Vargas-Gonzalez, L., Speyer, R., Campbell, J., 2010. Flexural strength, fracture toughness, and hardness of silicon carbide and boron carbide armor ceramics. *Int. J. Appl. Ceram. Tech.* 7, 643–651.
- Vaughan, B., Proud, W., Field, J., 2001. Shock properties of aluminum oxynitride. Tech. Rep. SP-1092, Cavendish Laboratory, Cambridge UK.
- Vogler, T., Clayton, J., 2008. Heterogeneous deformation and spall of an extruded tungsten alloy: plate impact experiments and crystal plasticity modeling. *J. Mech. Phys. Solids* 56, 297–335.
- Wallace, D., 1972. *Thermodynamics of Crystals*. John Wiley & Sons, New York.
- Wang, H., Ramesh, K., 2004. Dynamic strength and fragmentation of hot-pressed silicon carbide under uniaxial compression. *Acta Mater.* 52, 355–367.
- Warner, C., Hartnett, T., Fisher, D., Sunne, W., 2005. Characterization of AlON optical ceramic. In: *Proceedings of SPIE*, vol. 5786, Orlando FL, pp. 95–111.
- Wereszczak, A., Kirkland, T., Strong, K., Campbell, J., LaSalvia, J., Miller, H., 2010. Size-scaling of tensile failure stress in a hot-pressed silicon carbide. *Int. J. Appl. Ceram. Tech.* 7, 635–642.
- Wilkins, M., 1978. Mechanics of penetration and perforation. *Int. J. Eng. Sci.* 16, 793–807.
- Yuan, G., Feng, R., Gupta, Y., 2001. Compression and shear wave measurements to characterize the shocked state in silicon carbide. *J. Appl. Phys.* 89, 5372–5380.
- Zhang, D., Wu, M., Feng, R., 2005a. Micromechanical investigation of heterogeneous microplasticity in ceramics deformed under high confining stresses. *Mech. Mater.* 37, 95–112.
- Zhang, K., Wu, M., Feng, R., 2005b. Simulation of microplasticity-induced deformation in uniaxially strained ceramics by 3-D Voronoi polycrystal modeling. *Int. J. Plasticity* 21, 801–834.

NO. OF
COPIES ORGANIZATION

1 DEFENSE TECHNICAL
(PDF INFORMATION CTR
only) DTIC OCA
8725 JOHN J KINGMAN RD
STE 0944
FORT BELVOIR VA 22060-6218

1 DIRECTOR
US ARMY RESEARCH LAB
IMNE ALC HRR
2800 POWDER MILL RD
ADELPHI MD 20783-1197

1 DIRECTOR
US ARMY RESEARCH LAB
RDRL CIO LL
2800 POWDER MILL RD
ADELPHI MD 20783-1197

NO. OF
COPIES ORGANIZATION

ABERDEEN PROVING GROUND

46 DIR USARL
RDRL CIH C
P CHUNG
D GROVE
J KNAP
RDRL WM
B FORCH
J MCCAULEY
P PLOSTINS
RDRL WML B
I BATYREV
B RICE
D TAYLOR
N WEINGARTEN
RDRL WML H
B SCHUSTER
RDRL WMM
J BEATTY
RDRL WMM B
G GAZONAS
RDRL WMM E
C HILTON
J LASALVIA
J SINGH
J SWAB
RDRL WMP
S SCHOENFELD
RDRL WMP B
C HOPPEL
D POWELL
S SATAPATHY
M SCHEIDLER
T WEERASOORIYA
RDRL WMP C
R BECKER
S BILYK
T BJERKE
D CASEM
J CLAYTON (10 CPS)
D DANDEKAR
M GREENFIELD
R LEAVY
M RAFTENBERG
S SEGLETES
C WILLIAMS
RDRL WMP D
R DONEY
RDRL WMP E
S BARTUS
RDRL WMP F
N GNIAZDOWSKI

INTENTIONALLY LEFT BLANK.